Shape Tracking and Feedback Control of Cardiac Catheter Using MRI-Guided Robotic Platform—Validation With Pulmonary Vein Isolation Simulator in MRI

Ziyang Dong, Xiaomei Wang, *Member, IEEE*, Ge Fang, Zhuoliang He, Justin Di-Lang Ho, Chim-Lee Cheung, Wai Lun Tang, Xiaochen Xie, *Member, IEEE*, Liyuan Liang, Hing-Chiu Chang, Chi Keong Ching, and Ka-Wai Kwok, *Senior Member, IEEE*

***Abstract*—Cardiac electrophysiology is an effective treatment for atrial fibrillation, in which a long, steerable catheter is inserted into the heart chamber to conduct radio frequency ablation. Magnetic resonance imaging (MRI) can provide enhanced intraoperative monitoring of the ablation progress as well as the localization of catheter position. However, accurate and real-time tracking of the catheter shape and its efficient manipulation under MRI remains challenging. In this article, we designed a shape tracking system that integrates a multicore fiber Bragg grating (FBG) fiber and tracking coils with a standard cardiac catheter. Both the shape and positional tracking of the bendable section could be achieved. A learning-based modeling method is developed for cardiac catheters, which uses FBG-reconstructed three-dimensional curvatures for model initialization. The proposed modeling method was implemented on an MRI-guided robotic platform to achieve feedback control of a cardiac catheter. The shape tracking performance was experimentally verified, demonstrating 2.33° average error for each sensing segment and 1.53 mm positional accuracy at the catheter tip. The feedback control performance was tested by autonomous targeting and path following (average deviation of 0.62 mm) tasks. The overall performance of the integrated robotic system was validated by a pulmonary vein isolation simulator with *ex-vivo* tissue ablation, which employed a left atrial phantom with pulsatile liquid flow. Catheter tracking and feedback control tests were conducted in an MRI scanner, demonstrating the capability of the proposed system under MRI.**

***Index Terms*—Autonomous control, cardiac catheter, learning-based modeling, magnetic resonance imaging (MRI) guided catheterization, shape sensing.**

I. Introduction

CARDIAC electrophysiology (EP) is an effective treatment for atrial fibrillation. Electroanatomical mapping (EAM) and radio frequency (RF) ablation are two key procedures repeated in EP. The procedures require precise maneuvering of thin (∼Ø2.7 mm), long (∼1.2 m) and flexible catheters inside the heart chamber to measure electrical signals and deliver ablation energy. Magnetic resonance imaging (MRI) is a powerful imaging modality that has gained traction for guiding EP procedures [1], accredited to its superior high-contrast images of cardiovascular soft tissue and absence of harmful ionizing radiation. It can be used to form a detailed three-dimensional (3-D) cardiac roadmap, visualize physiological changes of cardiac tissues, and assess the ablation lesion formation intraoperatively [2], [3]. MR-based tracking [4], [5] could provide instrument localization under the same coordinate frame as imaging, avoiding any image registration that poses spatial error usually. Commercial MRI-guided catheterization systems (e.g., Imricor, ClearTrace, St. Jude Medical) have adopted active tracking coils for the positional feedback of catheter tip [3], [6], [7]. However, the sole use of discrete positional tracking coils could not provide precise information of the catheter morphology for either visualization or motion control. Although the catheter shape could be visualized by MRI [8], the prolonged time for image reconstruction would cause significant tracking delay. Accurate intraoperative (intra-op) shape tracking of catheters under MRI remains challenging.

Manuscript received October 24, 2021; accepted January 6, 2022. This work was supported in part by the Research Grants Council of Hong Kong under Grant 17206818, Grant 17205919, and Grant 17207020; in part by the Innovation and Technology Commission, Hong Kong under Grant MRP/029/20X; and in part by the Multi-Scale Medical Robotics Center Ltd. funded by ITC. This paper was recommended for publication by Associate Editor A. Krupa and Editor A. Menciassi upon evaluation of the reviewers' comments. *(Corresponding author: Ka-Wai Kwok.)*

Ziyang Dong, Ge Fang, Zhuoliang He, Justin Di-Lang Ho, Chim-Lee Cheung, Wai Lun Tang, Xiaochen Xie, and Ka-Wai Kwok are with the Department of Mechanical Engineering, The University of Hong Kong, Hong Kong (e-mail: ziyang.dong.matthew@gmail.com; fangge@hku.hk; hezl@connect.hku.hk; jdlho@connect.hku.hk; zardchim@hku.hk; at361836@hku.hk; xcxie@connect.hku.hk; kwokkw@hku.hk).

Xiaomei Wang is with the Department of Mechanical Engineering, The University of Hong Kong, Hong Kong, and also with the Multi-Scale Medical Robotics Center Ltd., Hong Kong (e-mail: wangxmei@connect.hku.hk).

Liyuan Liang is with the Department of Diagnostic Radiology, The University of Hong Kong, Hong Kong (e-mail: lyliang@connect.hku.hk).

Hing-Chiu Chang is with the Department of Diagnostic Radiology, The University of Hong Kong, Hong Kong, and also with the Department of Biomedical Engineering, The Chinese University of Hong Kong, Hong Kong (e-mail: hcchang@hku.hk).

Chi Keong Ching is with the Department of Cardiology, National Heart Centre, Singapore 169609 (e-mail: ching.chi.keong@singhealth.com.sg).

This article has supplementary material provided by the authors and color versions of one or more figures available at https://doi.org/10.1109/TRO.2022.3154691.

Digital Object Identifier 10.1109/TRO.2022.3154691

Optical fiber-based sensors using fiber Bragg gratings (FBGs) have attracted interest in measuring the morphological deformation of flexible surgical instruments. It can achieve real-time shape estimation with high sampling rates (>100 Hz) with thin, submillimeter diameters footprints. FBGs have excellent multiplexing capabilities, where many sensing points can be employed along with a fiber without increasing its size [9]. The use of multicore fibers with FBGs can further increase the sensor density and enable shape estimation of the fiber itself [10]. The flexibility of optical fiber also has minimal effect on the structural stiffness of the instrument, allowing it to be integrated with delicate devices, such as needles [11] and catheters. These distinctive advantages have prompted the use of FBGs in many applications, including navigation of medical instruments [12], [13], shape estimation and control of steerable interventional needles [14], [15], as well as force sensing to localize tissue hard-inclusions [16]. Researchers have attempted to integrate FBG optical fibers with catheters to achieve triaxial force sensing of catheter-tip-tissue interaction [17], demonstrating high sensing accuracy with miniaturized integration dimensions. Additionally, due to the inherent electromagnetic (EM) immunity optical fibers possess [18], FBG fibers are entirely compatible with MRI and have been demonstrated with MR safe/conditional instruments [19], [20].

Despite the increasing use of FBG for shape sensing, few studies have applied it to enhance the closed-loop control performance of surgical continuum manipulators [21], [22]. In the cardiac EP procedure, complicated and repeated tasks introduce difficulties to manual operation of catheters, even for experienced operators. It is expected that fast and accurate robot-assisted catheter positioning could significantly reduce operation times and difficulty when compared to manual operation [23], [24]. Previous studies have investigated various modeling/control methods to improve the accuracy and effectiveness of robotic catheter systems [25]–[27]. However, most of these catheters were custom-made with their known or deterministic structural parameters that enable precise modeling. For a standard cardiac catheter, its mechanical characteristics will vary due to manufacturing tolerances, inducing uncertainties in modeling and control. It creates strong incentive for utilizing shape sensing in robotic catheter control to achieve dexterous and precise manipulation, especially under MRI guidance.

In this article, we aim to develop a shape tracking method to provide both positional and morphological sensing of flexible cardiac catheter. To achieve accurate and effective feedback control, shape information obtained from the FBGs is used for the characterization of catheter kinematics as well as real-time autonomous control. The contributions are summarized as follows:

1) Design and implementation of a shape tracking system integrating a multicore FBG fiber and tracking coils with a standard cardiac catheter. Both shape and positional tracking of the bendable section could be achieved.
2) Development of a learning-based modeling method for cardiac catheters, which uses FBG-reconstructed 3-D curvatures for model initialization. The proposed modeling method was implemented on an MRI-guided robotic platform to achieve feedback control of a cardiac catheter.
3) Experimental validations of the shape tracking system and control algorithm. The overall robot control performance was demonstrated by targeting and path following tasks. An autonomous pulmonary vein isolation (PVI) task was conducted with *ex-vivo* tissue ablation inside a left atrial (LA) phantom with pulsatile liquid flow. Catheter tracking and feedback control tests were conducted in an MRI scanner, demonstrating the capability of the proposed system under MRI.

II. Shape Tracking With FBG Sensors

A. Shape Sensing With Multicore FBG Fiber

FBGs are sensors inscribed directly into optical fibers for measuring local, 1-D strain. Multiple FBGs can be inscribed along a single fiber to obtain strain sensing points without additional input or output connections. In our previous work [28], we designed a sensor capable of reconstructing its surface shape by embedding a single-core FBG fiber in a flexible substrate. However, for flexible and thin surgical instruments that are designed to access deep regions in the body, e.g., biopsy needles and cardiac catheters, a fiber with only a single core of FBGs is insufficient for reconstructing its 3-D curvature. Alternatively, multiple single-core fibers could be grouped [29] for colocated strain measurements. However, this would come at the cost of sensor size and ease of fabrication. A more reliable approach was to adopt a fiber fabricated with multiple optical cores (multicore fiber) and FBGs [10]. It allowed shape sensing of the fiber geometry itself while maintaining a thin cross-sectional size.

A quasi-continuous-grating multicore fiber (FBGS International) with optical frequency domain reflectometry (OFDR) interrogation (RTS125+, Sensuron) is used for shape sensing of the cardiac catheter. The fiber is 12 m long with a diameter of Ø0.2 mm. As in Fig. 1(b), seven cores run along the length of fiber, with one core centered around by other six cores equally spaced at 60° intervals. Shape sensing is achieved by measuring off-axis strain from the FBGs sensors located within the fiber cross section. Strain measurements could be obtained at the distal 1-m tip of the fiber with a spatial resolution of 3.17 mm. Note that the adopted multicore fiber features gratings with high spatial density; therefore, quasi-continuous strain measurement can be achieved [30], [31]. An OFDR-based system was used for the strain measurement, since it can provide a higher density of strain measurements along the short length of the catheter bending section. By contrast, the typical wavelength division multiplexing based fiber systems have *discretely* placed FBGs that are divided by bare fiber segments, with spacing between each FBG (spatial resolution) typically limited to around 10 mm [32].

There are two common approaches toward multicore fiber shape reconstruction from strain data: 1) Adopting the piecewise constant curvature (PCC) model with the assumption of circular bending shape for each segment of FBG. The overall fiber shape can be constructed by accumulating the sum of discrete curvatures and corresponding bending directions, which are measured and calculated from a set of sensors at a particular cross section of the fiber [33]. 2) Utilizing the Frenet–Serret formulas to describe 3-D curves, which can take account of the torsion effect [34].

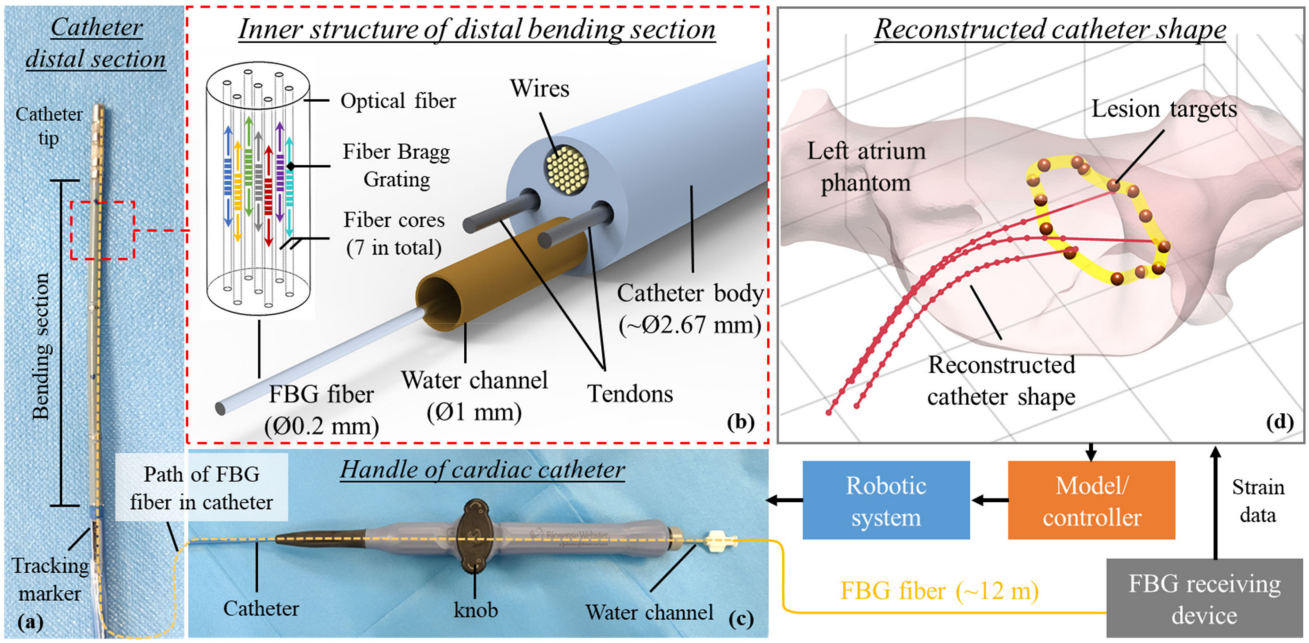

Fig. 1. Diagram showing the architecture of shape sensing for robotic catheter system. (a) Catheter distal bending section integrating a multicore FBG fiber (12 m long) and the tracking marker for shape tracking. (b) Inner structure of distal bending section, with multicore FBG fiber put throughout the water channel. (c) Handle of cardiac catheter, where the FBG fiber is fixed at the water channel entrance. (d) Real-time shape reconstruction can be achieved by continuously acquiring the strain data from FBGs. The 3-D curvature of the catheter bending section can then be feedback to the robotic catheter platform for autonomous control.

To optimize the reconstruction speed and sensing performance, the PCC-based approach is used in accredit to its faster convergence with respect to (w.r.t.) sensing segment length and superior noise handling ability [35]. For 3-D curvature reconstruction, at least three cores are needed to estimate the two-degree-of-freedom (2-DoF) section bending along the fiber cross section. More fiber cores could be employed to improve reconstruction accuracy and reduce overall sensing noise.

B. Fusing and Calibration of Shape and Positional Feedback

For shorter and more rigid instruments like biopsy needles, MR-based positional tracking markers can be located at a fixed base of the instrument to provide a reliable reference frame. However, this approach is not suitable for long (∼1.2 m) and *flexible* cardiac catheters, since its handle would be placed far from the MR imaging volume. In order to monitor the 3-D curvature of a standard cardiac catheter, as well as its tip position, the coordinate frame of the fiber's reconstructed curvature has to be coregistered with MR images. Note that the 3-D curvature reconstruction error can also be accumulated much along with the increasing sensing length.

To this end, we incorporate only the distal section of a multicore fiber to cover and feedback the catheter distal bending section with a length of 63.4 mm. For strain sensing of *i*th fiber core, the relationship between strain ε_i, curvature κ, and directional angle $(\varphi + \eta_i)$ from the neutral bending plane is described by the equation: $\varepsilon_i = -\kappa r_i \sin(\varphi + \eta_i) + e$ [21], where r_i is the distance of the *i*th core to the fiber center axis; φ and η_i are angles defined in the cross-sectional plane, respectively, which indicate the angle from the neutral bending plane to the first core, and the angle between the first core and the *i*th core $(\eta_1 = 0)$;e is the stretching-related strain offset in the fiber. In the equation, ε_i could be obtained from the sensor reading, whereas r_i and η_i are from the geometric configuration of fiber cores. When the geometry of the fiber cores is fixed, η_i could be obtained with φ remaining unknown. To calculate the unknown variables κ, φ, and e, at least three equations are needed, i.e., $i = 1, 2, 3$. Therefore, three cores are theoretically sufficient for shape reconstruction. And the seven-core FBG fiber provides redundancy for the measurement. The six cores around the center could be divided into two groups, each containing three cores to reconstruct the shape. Thus, the shape reconstruction accuracy could be improved by taking the average of the two shapes. In our test, the FBG fiber was placed within the water channel (Ø1 mm) inside an EP catheter (Thermocool, Biosense Webster Inc.) [see Fig. 1(a) and (c)], which has an outer diameter of 8-Fr (∼Ø2.67 mm). The water irrigation function would not be affected as the fiber diameter (Ø0.2 mm) is negligible relative to that of the water channel (Ø1 mm). Alternatively, the fiber could be integrated into the wire channel [see Fig. 1(b)] of the catheter in the future manufacture. To minimize the noise induced by fiber tip contact, the fiber was offset approximately 2 mm from the distal end and fixed at the water channel entrance to prevent sliding [see Fig. 1(c)].

Although the fiber can be used to reconstruct its 3-D curvature, the origin and orientation of the reconstructed shape are not defined within the robot or MRI coordinate system. In addition, as the fiber was fixed at the catheter handle, the catheter rolling could not be measured by the shape reconstruction. Therefore, we propose the use of real-time MR-based positional tracking coils that are integrated into the catheter to provide this

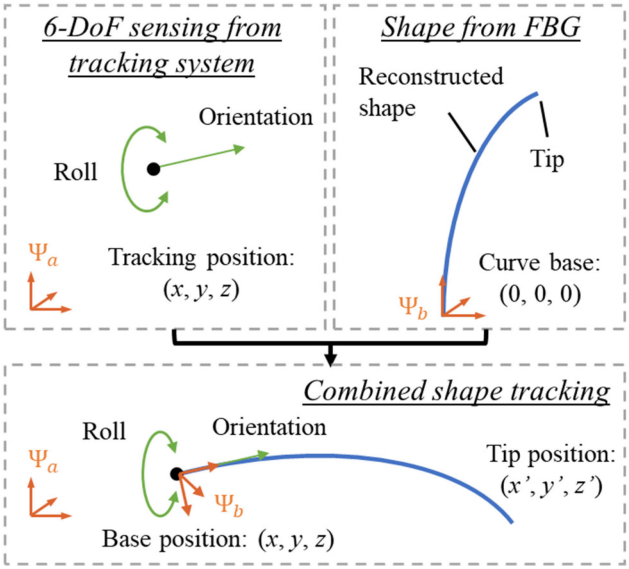

Fig. 2. Diagram illustrating the shape tracking method by *fusing* the 3-D curvature from FBG and positional sensing from the tracking coil.

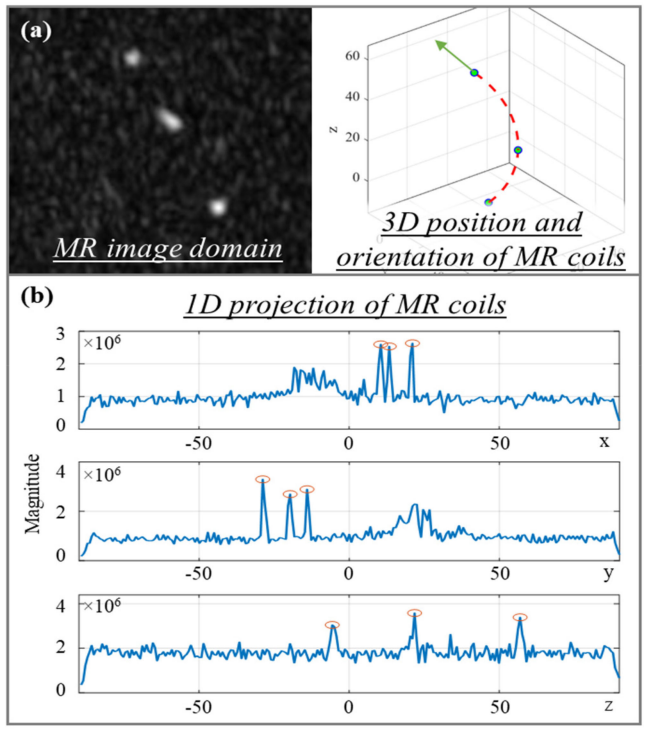

Fig. 3. (a) MR image revealing the MR tracking markers and the reconstructed 3-D positions from the 1-D projection pulse sequence. (b) 1-D projection of the three tracking markers along the orthogonal axes. Three RF signal peaks can be found in each projection.

information (see Figs. 2 and 16). Three coils located closely before the active bending section are expected to provide 6-DoF information in the MR imaging coordinate, and also map it to the catheter model. In our lab-based experimental validations, EM trackers and field generator (NDI Aurora) could be used as a comparable proxy for the MR-based tracking system. Preliminary validation of the MR tracking coils distributed along a catheter has been conducted and introduced in Sections II-C and V-G. The final output of the FBG-based shape tracking includes the curvatures and positions at each FBG segment along the sensing region, as well as the catheter tip position. For the learning-based PCC model, the curvatures and positions from the shape tracking are used to collect the training dataset to initialize the model parameters (see Section III-B). During the robot control, the shape tracking is used to locate the catheter tip and provide feedback data to control the catheter (see Section III-C).

Sensor calibration could be performed with the catheter bendable section placed in free space. The catheter was actuated to steer in opposite bending directions, whereas the FBG-reconstructed positions along the catheter bendable section were collected. The bending plane was generated by fitting through least squares of the normal distances, which we define as $\mathcal{P}_m$. Similarly, the bending plane generated by FBG-reconstructed points can be obtained as $\mathcal{P}_w$. The transformation to align $\mathcal{P}_w$ to $\mathcal{P}_m$ is then calculated via point-by-point optimization. For the tracking under MRI, as the tracking markers and FBG optic fiber are fixed on the catheter with known geometric relationship, the base position and orientation of FBG-reconstructed shape could be determined via matching the tracking markers' positions in MR images. In this way, the FBG-reconstructed shape can be registered with the MR tracking coordinates, thereby in the same MR image domain containing EAM. For the registration between the robotic frame and MR image frame, it will undergo the similar procedure.

C. Toward Shape Tracking Under MRI

MR tracking markers [36] can be used for 3-D localization of catheters under MRI. Active coil wired to the receiver system could realize a tracking resolution as high as 0.6×0.6×0.6 mm^3 [37]. MR-guided active tracking for cardiac EP has been demonstrated in RF ablation human trials, where active markers enabled real-time tracking and overlay of EP catheters on MR images [8]. Additionally, wireless multilayer markers [38]–[40] have potential to further simplify integration with catheters. Fabricated with amplifying circuits, MR tracking markers can provide high-contrast MR signal against anatomical surroundings, thus allowing positional localization in the MR image coordinate [see Fig. 3(a)]. The use of 1-D projection pulse sequence [41] allows acquisition of the marker positional signal along each axis, enabling fast localization up to 30 Hz. With an MRI real-time control interface, RTHawk (Heartvista), the raw scanning data can also be streamed out at low latency (<20 ms). The 1-D projection signals of three markers attached longitudinally and at different separations along a catheter body can be seen in Fig. 3(b). The peaks along each coordinate could be easily detected, and further back-projected to 3-D marker positions by matching the geometry constraints, e.g., distances between each marker pair. An arc was fitted to pass through the three markers and approximate the 3-D catheter shape [see Fig. 3(a)]. Benefiting from the small size and high accuracy (∼0.48 mm), three markers could be mounted on the catheter

in three separated circumferential directions in the future applications. The catheter orientation and rotation could be obtained by calculating the pose of cross-sectional triangle formed by the markers.

Compared to active coils that allow individual signal acquisition, wireless marker localization using 1-D projection sequence can produce singularities when peak overlap occurs on any of the axes. In this case, 2-D imaging interleaved with 1-D projection scans could be an alternative that allows detection of singularities and reconfirming of marker coordinates. However, this would come at the expense of sampling rate. The corresponding experiment with 2-D imaging was conducted in Section V-G.

III. Modeling and Control of Cardiac Catheter

A. Modeling of Catheters

We implemented the FBG shape tracking system on our previously developed MR safe catheter robot [42] (see Fig. 6), which is capable of teleoperating under intra-op MRI. The robot was designed to accommodate standard cardiac EP catheters. Detailed design and configurations of this robotic platform are introduced in Section IV-A. The steerable catheter can be regarded as a typical robotic continuum manipulator after being integrated into the actuation platform. To achieve accurate and effective autonomous control of catheters, particularly commercial ones, a reliable model is needed to provide precise motion mapping from the robotic actuator to the catheter tip.

Regarding modeling of the continuum manipulator, a common approach was to consider each of its bending sections as a constant-curvature arc [43]. The forward and inverse kinematic models can then be derived [44]. There are other more complex modeling approaches using beam theory [45] or Cosserat rod theory [46], mimicking a more realistic deflection but requiring longer computation time. However, for commercial cardiac catheters, the mechanical characteristics can vary due to manufacturing tolerances, which are difficult to be modeled using fixed parameters. It is also time-consuming and impractical to characterize the parameters of each cardiac catheter before use.

In view of this, we developed a modeling approach based on the assumption of PCC. The bendable distal shaft is modeled as a combination of n piecewise circular arcs, with curvatures represented by κ_i, $i = 1, 2, \ldots, n$. The distal section is assumed to deform in a plane determined by the two tendons. Regarding the base of the bendable section as the origin, we define the arc length s from the origin to a point on the bendable section, the angle between axis Z and tangent to the curve at that point as $\theta(s)$ (see Fig. 4). The arc length of each segment is l_i, $i = 1, 2, \ldots, n$. Without considering the rotation DoF, the catheter would bend in a fixed plane (x–z plane as in Fig. 4) w.r.t. the robot coordinate. According to Hasanzadeh and Janabi-Sharifi [27], the position of each point along the bendable section can be determined by

$$\begin{cases} x(s) = \int_0^s \sin\theta(\zeta)\, d\zeta \\ z(s) = \int_0^s \cos\theta(\zeta)\, d\zeta \end{cases} \tag{1}$$

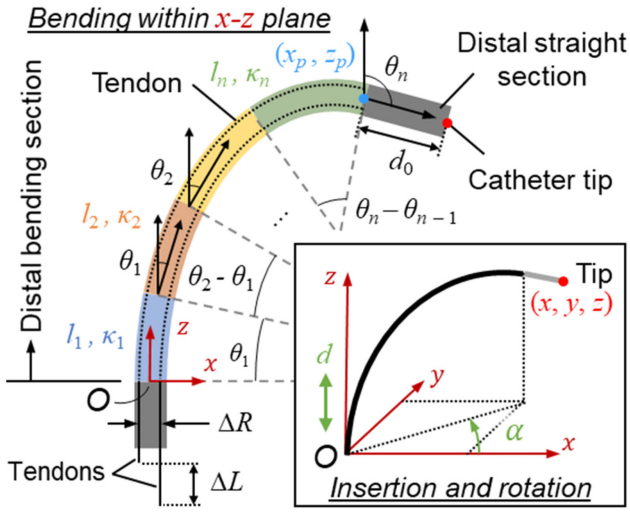

Fig. 4. Configuration of the catheter approximated by several curve segments. The curvature of the ith segment can be represented by κ_i. A straight section is added at the distal end on top of the PCC segments, which is the rigid tip of catheter.

where the angle $\theta_i(s)$ on the ith segment is

$$\theta_i(s) = \kappa_i s + \sum_{j=1}^{i-1} l_j(\kappa_j - \kappa_i) \tag{2}$$

where κ_0=0 at the origin. The position (x_p, z_p) of bendable section end on the bending plane without rotation can be calculated based on (1) as

$$\begin{cases} x_p = \sum_{i=1}^{n} \int_{a_i}^{b_i} \sin\theta_i(\zeta)\, d\zeta \\ z_p = \sum_{i=1}^{n} \int_{a_i}^{b_i} \cos\theta_i(\zeta)\, d\zeta \end{cases} \tag{3}$$

where the lower and upper limits of integration are, respectively

$$a_i = \sum_{j=0}^{i-1} l_j \text{ and } b_i = \sum_{j=0}^{i} l_j, i = 1, 2, \ldots, n. \tag{4}$$

Substituting (2) into (3) and defining $l_0 = 0$, the final expression of position (x_p, z_p) can be obtained.

The constant length of distal straight tip is defined as d_0, and the insertion distance and rotation angle of end-effector as d and α, respectively. Thus, the spatial position $\boldsymbol{p} = (x, y, z)$ of catheter end-effector in a coordinate as in Fig. 4 could be represented as

$$\begin{cases} x = (x_p + d_0 \sin\theta_n)\cos\alpha \\ y = (x_p + d_0 \sin\theta_n)\sin\alpha \\ z = z_p + d_0\cos\theta_n + d \end{cases}. \tag{5}$$

The catheter deformation is determined by the relative position of two tendons. Here, we represent the distance between two tendons as ΔR. The tendons are pulled and pushed by the knob on the catheter handle, whose radius is represented by r_{cam} and steering angle by ϕ (i.e., the rotation angle of steering knob [47]). A relationship based on the representation of tip bending

angle θ_n can be obtained as

$$\theta_n = \sum_{i=1}^{n} \kappa_i l_i = \frac{2 \cdot r_{cam} \sin\phi}{\Delta R} = \frac{\Delta L}{\Delta R} \tag{6}$$

where the axial displacement difference between the two tendons is ΔL.

To this end, the mapping between configuration and task spaces is derived [48], i.e., the relationship between catheter tip position and bending curvatures κ_i, $i = 1, 2, \ldots, n$. However, for the bending DoF of robotic catheter, the mapping between actuation space and configuration space is still unknown, that is, the relationship between knob rotation ϕ and bending curvatures κ_i, $i = 1, 2, \ldots, n$. We aim to find the mapping from ϕ to each κ_i, as well as resolve the unmodeled characteristics by a learning-based method. Therefore, the kinematics between actuation and task spaces could be established.

B. System Characterization With a Learning-Based Method

As described in Section III-A, the forward model would be established only in the condition that all the segment curvatures or their ratios are available. We define the curvature ratio as

$$\boldsymbol{k}_c = \left[k_{c1} \; k_{c2} \; \cdots \; k_{cn} \right]^{\mathrm{T}}, \sum_{i=1}^{n} k_{ci} = 1. \tag{7}$$

In the PCC model, ΔL from (6) could also be divided into n elements and represented as a vector in the following form:

$$\Delta \boldsymbol{l} = \left[\Delta l_1 \; \Delta l_2 \; \cdots \; \Delta l_n \right]^{\mathrm{T}}, \Delta L = \sum_{i=1}^{n} \Delta l_i \tag{8}$$

where $\Delta \boldsymbol{l}$ is proportional to the curvature ratio $\boldsymbol{k}_c$. A learning-based method is adopted to obtain the curvature ratio among all the segments.

Aforementioned in Section II-A, the multicore FBG fiber can reconstruct the curves by approximately consecutive points. The 3-D positions and the radii between adjacent points can both be obtained, represented by $\boldsymbol{p}_j^s, j = 1, 2, \ldots, M$ and $r_j^s, j = 1, 2, \ldots, M - 1$, respectively, where M is the total number of effective points in the reconstruction. Positions and radii at time step k are $\boldsymbol{p}_j^s(k)$ and $r_j^s(k)$, respectively. Corresponding to the segmentation in PCC model, each segment's curvature $\kappa_i(k), i = 1, 2, \ldots, n$ (see Section III-A) can be obtained as the reciprocal of the average radius. The knob steering angle at time step k is $\phi(k)$, which drives the catheter tendon displacement. The curvatures from FBG shape reconstruction can be regarded as ground truth, and used to train the mapping between the steering angle $\phi(k)$ and the curvature ratio $\boldsymbol{k}_c$.

Besides the multisegment curvatures, we also consider the hysteresis resulting from friction and/or tendon looseness. The backlash will appear particularly when changing bending direction (i.e., steering direction of the knob). Differences between the analytical model and actual bending performance can be compensated by imposing additional input compensator l_c to the ΔL during the robot manipulation.

Therefore, the actual relative position after the learning-based compensation can be calculated by

$$\Delta \boldsymbol{l} = \boldsymbol{k}_c \cdot (\Delta L + l_c). \tag{9}$$

The parameters to be trained are $\boldsymbol{k}_c$ in (7) and l_c, corresponding to the specific knob steering angle ϕ.

Training: In the pretraining procedure, the radii $r_j^s, j = 1, 2, \ldots, M - 1$ at each time step has to be collected, as well as the motor's position $q(t)$ that is correlated to the knob steering angle $\phi(t)$. To cover the whole bending workspace, the knob is rotated with a predefined actuation sequence

$$\boldsymbol{Q} = \left[q(1) \; q(2) \; \cdots \; q(N) \right] \tag{10}$$

where N is the sampling number. A value $s(t)$ is introduced to represent the actuation direction change between current and previous steps, which can be derived as

$$s(t) = \mathrm{sign}\left(q(t) - q(t-1)\right), t = 1, 2, \ldots, N \tag{11}$$

where the function $\mathrm{sign}(\cdot)$ is to differentiate positive and negative values. The sequence of curvatures could be obtained as

$$\boldsymbol{C} = \left[\boldsymbol{c}(1) \; \boldsymbol{c}(2) \; \cdots \; \boldsymbol{c}(N) \right] \tag{12}$$

where $\boldsymbol{c}(t) = \left[c_1(t) \; c_2(t) \; \cdots \; c_n(t) \right]^{\mathrm{T}}$ and $c_i(t)$ is the curvature of the ith segment in accord with Section III-B. The curvature ratio in (7) could be obtained by normalizing $\boldsymbol{c}(t)$.

The parameter l_c could be derived based on the tip bending angle θ_n, which is independent of $\Delta \boldsymbol{l}$ and could be calculated from ΔL. For each actuation input, the actual tip bending angle θ_A can be obtained from the FBGs, whereas the predicted tip bending angle θ_P can be calculated from the forward PCC model. Thus, a compensation-related parameter f_c is available for training

$$f_c = \exp\left(\Delta R \cdot (\theta_A - \theta_p)\right). \tag{13}$$

The input of training data is

$$\boldsymbol{U} = \left[\boldsymbol{u}(1) \; \boldsymbol{u}(2) \; \cdots \; \boldsymbol{u}(N) \right] \tag{14}$$

where

$$\boldsymbol{u}(t) = \left[q(t) \; s(t) \right]^{\mathrm{T}}, t = 1, 2, \ldots, N. \tag{15}$$

The output of training data is

$$\boldsymbol{O} = \left[\boldsymbol{o}(1) \; \boldsymbol{o}(2) \; \cdots \; \boldsymbol{o}(N) \right] \tag{16}$$

where

$$\boldsymbol{o}(t) = \left[\boldsymbol{k}_c(t)^{\mathrm{T}} \; f_c(t) \right]^{\mathrm{T}}, t = 1, 2, \ldots, N. \tag{17}$$

Using the feedforward neural network in the deep learning toolbox of MATLAB, with $\boldsymbol{U}$ as input and $\boldsymbol{O}$ as output, we can train a mapping as

$$\boldsymbol{o}(t) = f\left(\boldsymbol{u}(t)\right), t = 1, 2, \ldots, N. \tag{18}$$

This feedforward neural network has one hidden layer with 60 neurons. The input data was separated into three groups for training, validation and test, with a ratio of 0.8: 0.1: 0.1. The network used log-sigmoid transfer function for hidden layers and linear transfer function for output layer. Bayesian regularization backpropagation was used as the network training function.

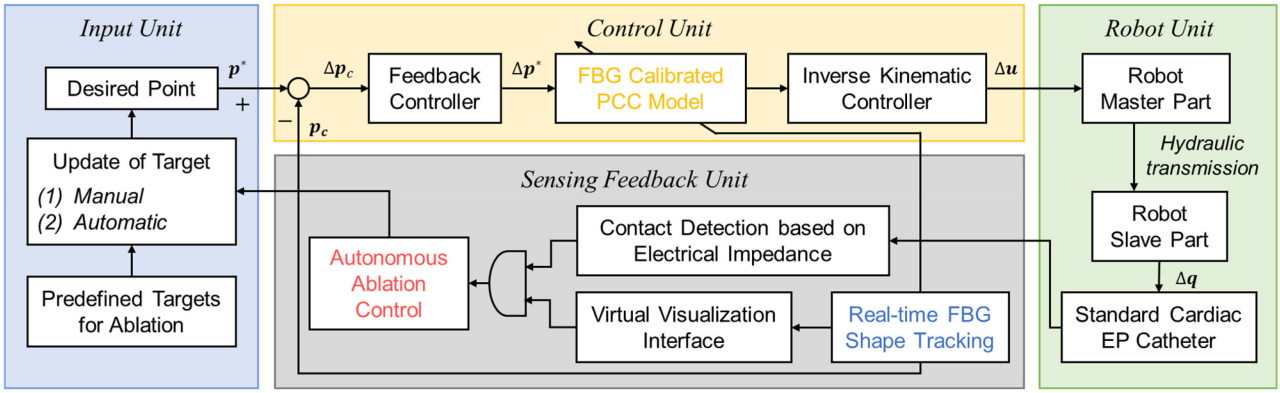

Fig. 5. Control architecture of the autonomous ablation procedure. Parameters (curvature ratio $\boldsymbol{k}_c$ and input compensator l_c) of the PCC model (yellow texts) could be automatically initialized and tuned by a learning-based algorithm, which enables accurate positional control of the catheter end-effector. The tip position and 3-D curvature of catheter could be obtained in real time from the FBG-based shape tracking method (blue texts). RF ablation (red texts) would be triggered when the catheter tip reaches the target and contacts tissue.

Prediction: During robot motion, the curvature ratio $\boldsymbol{k}_c(k)$ among different segments and the compensation-related $l_c(k)$ at the kth step can be calculated by

$$[\boldsymbol{k}_c(k), f_c(k)] = f(q(k), s(k)), k = 1, 2, \ldots. \tag{19}$$

The enhanced estimation of relative positions between two tendons $\Delta\boldsymbol{l}$ can be calculated by (8), where $l_c(k)$ can be derived as

$$l_c(k) = \ln(f_c(k)). \tag{20}$$

The predicted $\boldsymbol{k}_c$ and l_c would link up ϕ and κ_i, i = 1, 2, …, n, completing the mapping between actuation and configuration spaces of bending DoF. Combined with (5), the complete forward kinematics is available for robotic control

$$\dot{\boldsymbol{p}} = \boldsymbol{J}\left[\dot{\alpha}\ \dot{\phi}\ \dot{d}\right]^{\mathrm{T}} \tag{21}$$

where $\boldsymbol{J}$ is the Jacobian matrix, which can be calculated by

$$\boldsymbol{J} = \begin{bmatrix} \frac{\partial x}{\partial \alpha} & \frac{\partial x}{\partial \phi} & \frac{\partial x}{\partial d} \\ \frac{\partial y}{\partial \alpha} & \frac{\partial y}{\partial \phi} & \frac{\partial y}{\partial d} \\ \frac{\partial z}{\partial \alpha} & \frac{\partial z}{\partial \phi} & \frac{\partial z}{\partial d} \end{bmatrix} \tag{22}$$

based on the forward kinematic expression in (5). In the learning-based model, the no-solution case of inverse kinematics due to zero curvature is resolved by manually adding a sufficiently small value into the curvature (e.g., 10^{-6} mm^{-1}), which could ensure the continuous iteration of the control loop.

C. Autonomous Motion Control and Ablation

For the task of autonomous ablation, targets in the model coordinates $\{\boldsymbol{C}\}$ are predefined around the pulmonary vein ostium in the phantom. The real-time tip position $\boldsymbol{p}_w$ could be provided by the shape tracking system in the world coordinates $\{\boldsymbol{W}\}$. $\boldsymbol{p}_c$ and $\boldsymbol{p}_w$ are transformed using the rotation matrix $\boldsymbol{R}_w^c$ and translation vector calculated by registration approach.

During each targeting cycle, the target could be appointed either automatically in sequence or selected by the operator. The error between current tip position $\boldsymbol{p}_c$ and desired position $\boldsymbol{p}^*$ would be calculated and normalized with constant step size as $\Delta\boldsymbol{p}_c$. The feedback controller will normalize the desired motion with proper step size. The inverse kinematic controller calculates the actuation change corresponding to the desired tip movement, which is represented by $\Delta\boldsymbol{p}^*$, using the updated Jacobian matrix. The robot actuation is derived by multiplying the Jacobian matrix and $\Delta\boldsymbol{p}_c$. A tolerance distance from the catheter tip would be set for each target. The ablation process would be automatically triggered by simultaneously satisfying the two conditions: 1) tissue contact is detected with an appropriate impedance for ablation (e.g., $< 200\ \Omega$ [49]); 2) targeting error is within the tolerance distance. During the ablation process, the robot would keep still for RF ablation on the tissue. The control block diagram in Fig. 5 shows the key processing components including the kinematic control and autonomous ablation.

IV. Experimental Setup

A. MR Safe Robotic Catheter Platform

The proposed shape sensing method and control algorithms are implemented, and then evaluated on an MR safe robotic catheter system [42], [50] (see Fig. 6), which is capable of teleoperating the catheter inside MRI scanner bore. The robot features a master-slave hydraulic transmission system in order to provide high-accuracy and low-latency actuation. The master units are driven by electric motors located in the control room. Actuation from master units can be transmitted to the slave units through 10-m-long hydraulic pipelines. The robot can manipulate a standard EP catheter (Thermocool Bi-Directional Catheter, Biosense Webster Inc.) in three DoFs, namely bending, insertion, and rotation. Motion ranges of each DoF are summarized in Table I. The catheter has a length of 115 mm and outer diameter of 8-Fr (∼Ø2.67 mm). For other standard EP catheters with different lengths, a similar manipulation performance is expected, since their bending segments will only be maneuvered after the transseptal puncture.

The robotic system is upgraded from the previous prototype [42], incorporating our previously designed three-cylinder actuation units [51] for rotation and insertion DoFs of the catheter. It enables a large motion range for catheter advancement (340

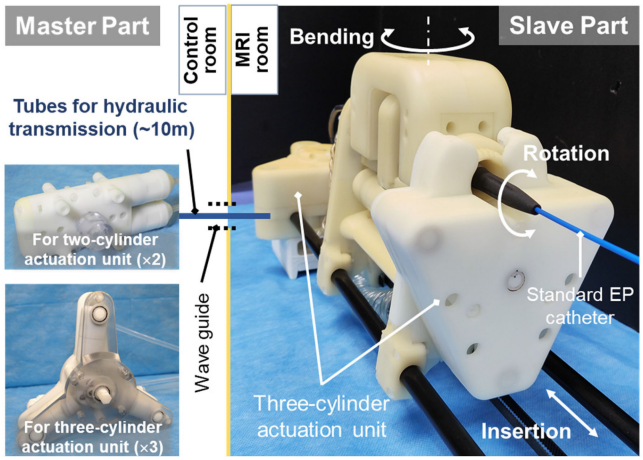

Fig. 6. MR safe robotic catheter platform providing the 3-DoF manipulation (bending, rotation, and insertion) of standard cardiac EP catheter.

TABLE I
SPECIFICATION OF THE ROBOTIC CATHETER PLATFORM

Size	800×140×210 mm^3
Hydraulic transmission	
Pipeline	Length: 10 m; Outer/Inner diameter: 6/4 mm (Nylon: DG-5431101, Daoguan Inc.)
Pressure	0.1 MPa
Rolling diaphragm	Type 1: Diameter - 18 mm, Stroke - 35 mm Type 2: Diameter - 10 mm, Stroke - 20 mm
Motion range	
Bending	-60° ~ 60° (at catheter tip)
Rotation	-360° ~ 360°
Insertion	0 ~ 340 mm

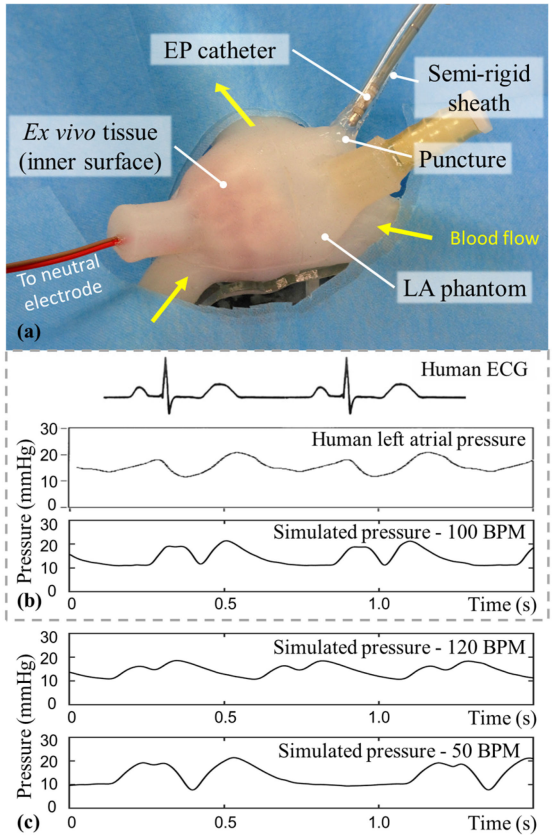

Fig. 7. (a) LA phantom filled with liquid, of which the pulsatile flow was generated by a hydraulic pump. A slice of swine tissue was attached on the inner surface at target ablation area. (b) Simulated liquid pressure compared to the human ECG and LA pressure. (c) Simulated pressures in LA phantom with fast and slow rates. The pulsatile rate could be adjusted within the range.

mm) and rotation (±360°), as well as high-fidelity catheter manipulation. Such improved robotic actuation performance would enable feedback control implementation for effective autonomous catheter manipulation, thereby delicate cardiac EP tasks, such as EAM and RF ablation.

B. *LA Phantom With Pulsatile Flow and* Ex-Vivo *Tissue*

To perform a simulated PVI task, an LA phantom model was designed based on patient-specific imaging data [see Fig. 7(a)]. The phantom was molded by silicone [52] in attempt to mimic the LA tissues consisting of myocardium and endocardium. A semirigid sheath was fixed at the puncture on phantom wall, simulating a path along the femoral vein, inferior vena cava, right atrium to left atrium. Pulsatile liquid flow can be generated by a water pump through pipelines to the LA phantom. The flow direction is indicated by the arrows in Fig. 7(a), which follows the LA blood flow from pulmonary veins to left ventricle. The LA pressure and resultant motion during EP procedure could be simulated by controlling the magnitude and frequency of pulsatile flow, which could be gated with the patient-specific electrocardiogram (ECG) signal. Fig. 7(b) shows the simulated liquid pressure compared to the human ECG and LA pressure [53], [54]. Fig. 7(c) shows the simulated pressure curves at fast and slow pulsatile rates. The rates could be adjusted within the range, covering the common patient heartbeat rate during EP procedure.

To conduct the *ex-vivo* tissue ablation, a slice of swine tissue with 3 mm thickness was attached on the phantom inner surface around pulmonary veins. In EP procedure, a neutral electrode is usually attached on patient's body to form a close electric circuit with catheter and RF generator, in order to monitor tissue resistance and conduct RF ablation. In this setup with LA phantom, the *ex-vivo* tissue was linked to a neutral electrode through electrical wires, which was connected to an RF generator (Biosense Webster Stockert 70). The control program was gated with the generator to automatically trigger the RF ablation when the catheter tip reached the target range and contacted the tissue.

V. PERFORMANCE EVALUATION

A. *Shape Sensing Performance of the Multicore FBG*

To validate the FBG shape sensing performance when integrated with the cardiac catheter, a fixed curvature test was conducted on the two symmetric bending curvature templates, as shown in Fig. 8(a). The templates were 3-D printed with fixed curvature grooves of 2.7 mm width, which is approximately equal to the outer diameter of EP catheter. The bending angles

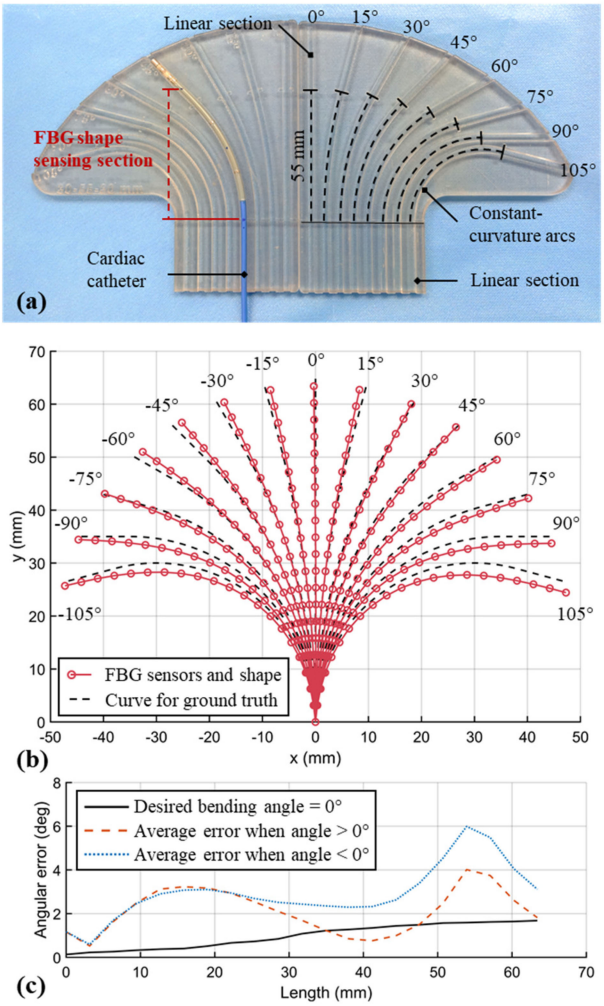

Fig. 8. (a) Bending curvature templates used to evaluate the shape sensing performance of the multicore FBG fiber. Eight curvatures are included at each bending direction, with an absolute value from 0° to 105°. (b) Reconstruction catheter shapes compared with the ground truth curves. The starting positions are all aligned at (0,0). (c) Bending angle errors along the shape sensing section.

of the curved section are from 0° to 105° on each side. The length of the constant-curvature arc section is 55 mm. The integration of FBG and cardiac catheter followed the method in Section II-A. The shape of 63.4 mm distal catheter section was reconstructed by three cores in the fiber, with each core containing 21 FBG segments. The catheter was placed into the template grooves for measuring its 3-D curvature. For each measurement, the location of first FBG segment was aligned to the start position of the constant-curvature arcs. The reconstructed 3-D curvature was obtained by taking average of 100 consecutive data captures for the entire sensing section.

The reconstructed catheter shapes are plotted in Fig. 8(b), with the position of first FBG section set as the origin (0,0). Curves for the ground truths are also plotted, following the same shape of corresponding grooves. The overall average angular error of all FBG sensors is 2.33°. And the average tip bending angle is 2.35° for all curvatures. Fig. 8(c) illustrates the average errors of the tip bending angle in different groups of predefined bending angle. Other than the sensor error of FBGs, the misalignment between the reconstructed shape and ground truth could be partially attributed to the large gap between the FBG fiber (Ø0.2 mm) and the water channel (Ø1 mm). In future manufacture, the fiber could be put through a sheath with slightly larger diameter to minimize such interspace, thus to improve the overall sensing accuracy. The sheath could also be integrated into the wire channel of catheter for to free up the water channel for irrigation function.

As for the shape reconstruction error induced by temperature change, it would appear if a set of FBGs at the fiber's cross section experienced measurable differences in temperature. However, for the seven-core FBG fiber with close proximity of each core, any local temperature changes on the fiber during surgery would produce a negligible temperature gradient across a fiber cross section [55], particularly if the fiber is protected within the catheter channel. For extreme cases with large temperature variation, the center (unstrained) core of the multicore fiber could be used for temperature compensation [56]. From our observations, the shape reconstruction accuracy was not affected even when the catheter was placed into water with differing temperatures (∼25 °C and ∼37 °C).

B. Shape Tracking Under Active Bending

The shape tracking performance was further evaluated with active catheter manipulation. The integration method of FBG fiber with the catheter remained the same as in Section V-A. A 6-DoF EM positional sensor (Ø0.8×9 mm, NDI Medical Aurora) was attached to the catheter at the location of first FBG sensor. Before data collection, the coordinate frames of the reconstructed shape and EM tracking system were aligned following the procedure in Section II-B. During the test, the cardiac catheter was actuated by the robotic platform for bending in two directions. The shape and positional data of the catheter were recorded under seven knob steering angles, which are summarized in the table in Fig. 9(a). For each input angle, the 3-D curvature for ground truth is represented by 25 evenly distributed points, which were captured along the catheter by an EM tracking probe (NDI Medical Aurora).

The diagrams in Fig. 9(a) depict shapes of the catheter bending section under seven knob steering angles, which were periodically repeated for five cycles. For each input, the mean reconstructed catheter shape is represented by a red curve, whereas the error band is overlaid as a red shaded area. To account for the rigid section of the catheter tip and obtain the catheter tip position, a 14 mm straight section was added to the distal end of the reconstructed 3-D curvature based on the orientation of the last FBG segment. The root-mean-square error and the standard deviation of the FBG-reconstructed tip position for the five measurements are summarized in the table in Fig. 9(a).

Simulated shapes deduced by the learning-based model in Section III-B are also overlaid in the diagram, predicting similar shapes and positions to the measured results. The side view of the shape tracking curves is plotted in Fig. 9(a), indicating that the catheter used for the experiment has a nearly planar bending behavior. The reconstructed shapes from FBG fiber are consistent with the real shape, implying there is no significant twist between

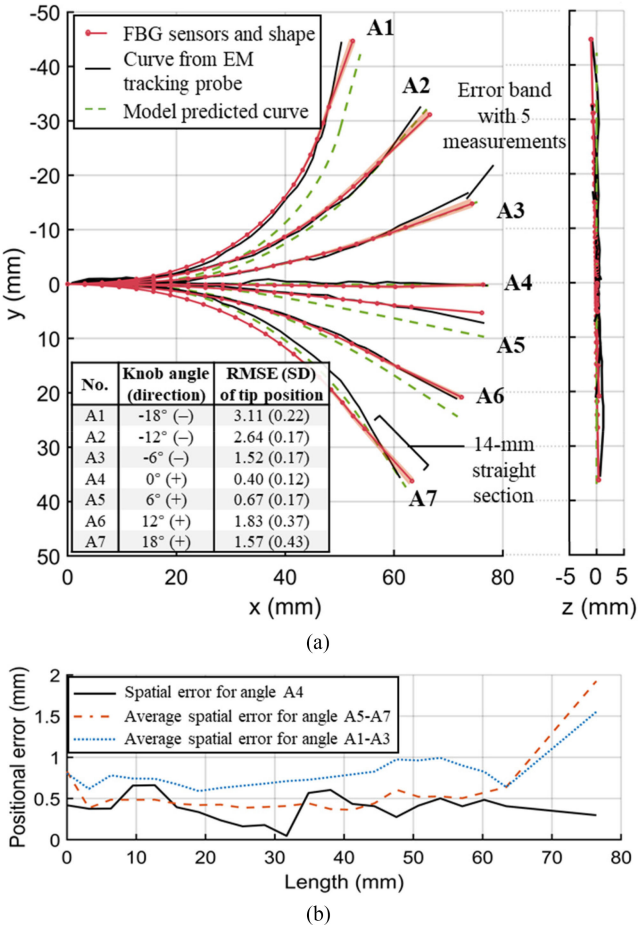

No.	Knob angle (direction)	RMSE (SD) of tip position
A1	-18° (–)	3.11 (0.22)
A2	-12° (–)	2.64 (0.17)
A3	-6° (–)	1.52 (0.17)
A4	0° (+)	0.40 (0.12)
A5	6° (+)	0.67 (0.17)
A6	12° (+)	1.83 (0.37)
A7	18° (+)	1.57 (0.43)

Fig. 9. (a) Top and side views of catheter shapes obtained from FBG shape sensing (red curves: mean curvature, red shaded area: error band), EM tracking system (black), as well as model prediction (green). The catheter was actuated by the robotic platform with seven knob steering angles, which were also used for model input. (b) Spatial differences along the shape sensing section by comparing the curves from FBGs and the EM tracking system.

the FBG fiber and the catheter. The spatial positional errors of shape tracking for the bending section are shown in Fig. 9(b). The average positional error of 21 FBG sensing segments is 0.63 mm, and 1.53 mm at the tip. The largest tip error is 2.27 mm for A7, which is within the tolerance of targeting error (∼5 mm [57]) in EP procedures.

C. Learning-Based PCC Versus Constant Curvature (CC)

The proposed learning-based PCC model was compared to the conventional CC model by simulation. The CC model refers to a spatial arc with a constant curvature along the whole structure. The difference between CC and PCC is whether the arc is segmented as multiple sections in constant curvatures. The structure-related parameters of the two models (e.g., length, diameter) were set to be identical. In the PCC model, we divided the bendable section into three segments (i.e., $n = 3$ in Section III-A) for ease of calculation and analysis. The knob steering angles ϕ in a range of –20° to 20° were input to both models. For the proposed learning-based PCC model, the actuation direction $s(t)$ is also considered as an input, as introduced in (11).

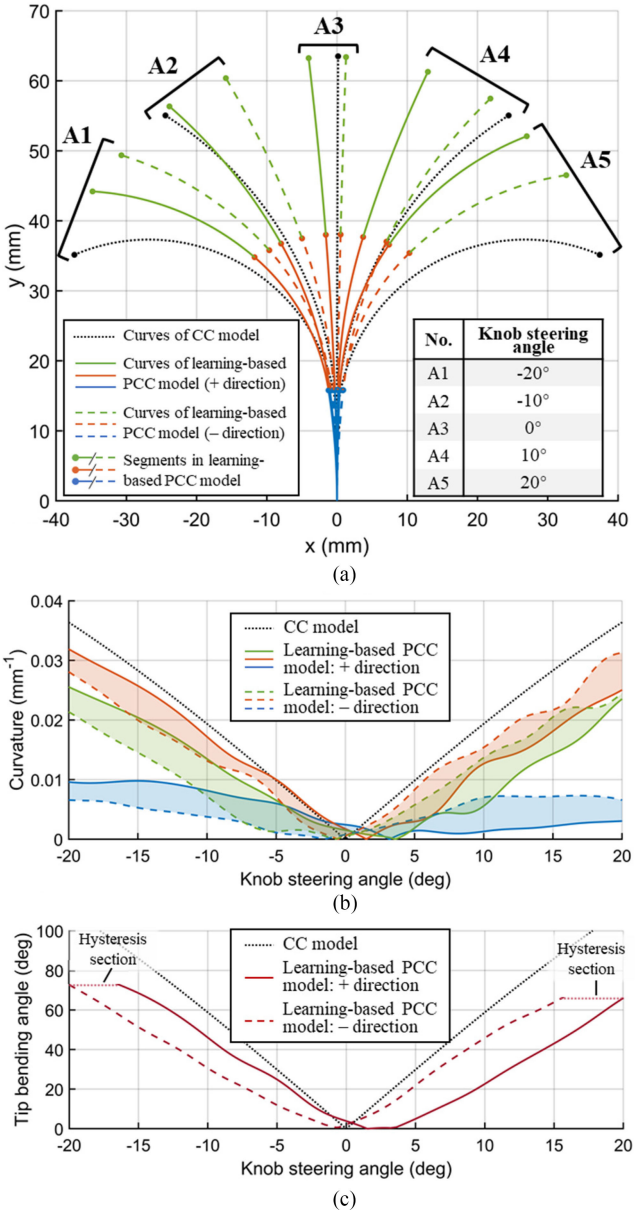

No.	Knob steering angle
A1	-20°
A2	-10°
A3	0°
A4	10°
A5	20°

Fig. 10. (a) Simulated catheter bending curves by the CC model and the learning-based PCC model with five knob steering angles (A1–A5). (b), (c) Diagrams showing the curvature and tip bending angle variation trends for CC model and learning-based PCC model. The learning-based PCC model can predict the actuation hysteresis with including the actuation direction.

Fig. 10(a) illustrates the simulated catheter planar curves with five inputs of knob steering angle, A1–A5. For the learning-based PCC model, each knob angle could generate two curves in two actuation directions, namely positive (+) and negative (–). The variation trends of curvature and tip bending angle are depicted in Fig. 10(b) and (c), respectively, w.r.t. the knob steering angles. The CC model exhibits a linear increase with a larger magnitude in both cases. As for the learning-based PCC model, a nonlinear relation between the knob input and curvatures of three segments could be predicted, as well as the tip bending angle. These predictions conform with the observed bending behavior of commercial cardiac catheters, which could be attributed to the

tendon-sheath friction, manufacturing tolerance, and nonideal material conditions.

The learning-based PCC model could also reveal the bending hysteresis of catheter by involving the actuation directions. As illustrated in Fig. 10(c), the tip bending angle would follow the solid (/dashed) curve when the knob steering angle is increasing (/decreasing), corresponding to the + (/–) actuation direction. The flat sections horizontally connect the two curves in opposite actuation directions, which represent the hysteresis of the catheter manipulation. The hysteresis could be predicted for every knob input within the actuation range. During the robot control, if the actuation direction changes, the model-predicted output will be horizontally transited to another curve directly, without staying in the hysteresis section. Thus, from the inverse model, a new knob steering angle could be obtained and given to the robot, which contains the hysteresis compensation value. Note that such compensation is relatively small for motors' actuation, which could complete the transition without any delay. In this way, Jacobian calculation will not be affected by the hysteresis sections, as the Jacobian matrix will only be deduced based on the inverse model represented by the two curves.

D. Autonomous Targeting

An autonomous targeting experiment was carried out by implementing the proposed shape tracking and learning-based modeling on the robotic platform. Five targets [T1–T5 in Fig. 11(a)], which are in a volume of 78.4×75.7×46.3 mm^3, were chosen within the workspace of catheter tip. The EP catheter passed through a polytetrafluoroethylene (PTFE) pipeline with 0.8 m length and 4 mm inner diameter, which started at the robotic platform and ended before the catheter bendable section. The catheter's bending section could move freely in the workspace. The PTFE pipeline simulated a path along the vessel to heart chamber. During the task, the catheter was *automatically* manipulated by the robotic platform to reach the targets in a sequence from T1 to T5. The tip position and catheter shape were recorded and fed back by the proposed shape tracking method. The pretrained catheter model introduced in Section V-C was used to control the robot.

The footprint of catheter tip during autonomous targeting is shown in Fig. 11(a), with the trajectories represented by different colors. The red curves with dots indicate the reconstructed catheter shape and position when its tip reached the targets. The deviations from the tip to targeting points during the five stages are illustrated in Fig. 11(b). The average duration toward each target is 16.9 s, with the maximum duration of 25.8 s (T3). The longer duration toward T3 could be attributed to the larger targeting distance (85.8 mm), as the tip maximum speed was limited in the control algorithm to ensure a safe catheter manipulation. The results indicate a fast and efficient autonomous targeting performance of the robotic system incorporating with the shape tracking and control systems.

E. Path Following

To further investigate the overall feedback control performance of the robotic catheter system, a path following task was

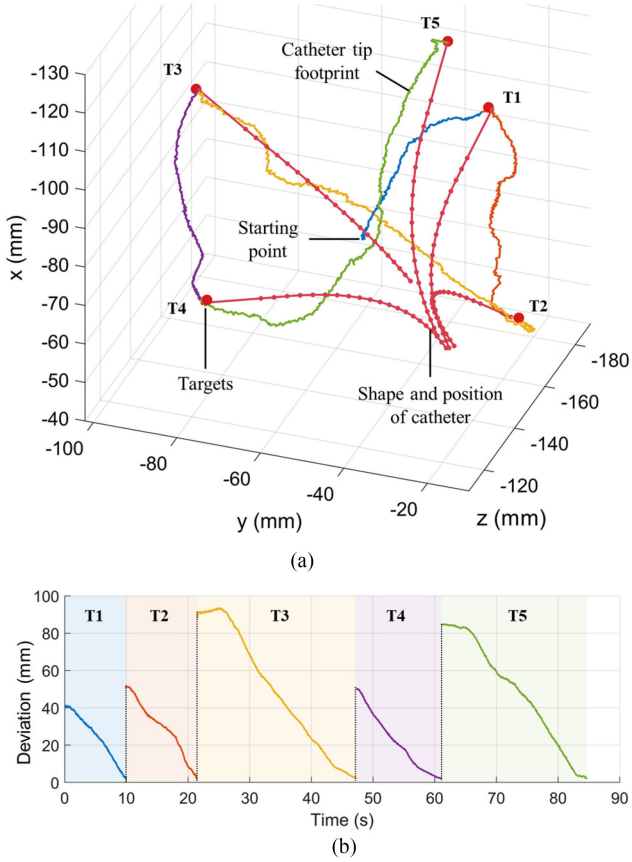

Fig. 11. (a) Diagrams showing the catheter tip trajectory toward the five targets during the autonomous targeting. The reconstructed catheter shape and position were plotted for the instances when the tip reached the targets. (b) Deviation from the tip to the targets during the five stages.

conducted. The static reference path was predefined in the shape of a sideways figure eight ("∞"), which has a dimension of 60×30 mm^2. The learning-based PCC model was implemented on the robot. The catheter tip was autonomously controlled to trace the reference path periodically, with the duration of each loop set to 60 s.

The diagram in Fig. 12(a) depicts the tip footprint recorded by the shape tracking system over five cycles. The deviation from the tip to the reference curve is indicated by the warm color gradient. Fig. 12(b) illustrates the corresponding tip deviation over the five tracing cycles. A mean value of deviation, 0.62 mm, could be found throughout the trajectory after the approaching stage. Most segments of the trajectory tracking are smooth and closed along with the reference curve. Several sections of the tip footprint have greater deviations (max. 2.34 mm), which is mainly due to the backlash and nonlinearity of the catheter manipulation and robotic actuation. The reconstructed curves of the catheter are also overlaid on the diagrams as red curves with dots, representing the instantaneous shape and position of the bending section at 12, 24, 36, 48, and 50 s during the first cycle. A close tracing between the tip footprint and reference curve could be clearly observed in Fig. 12(c), together with the reconstructed catheter shapes in various bending curvatures.

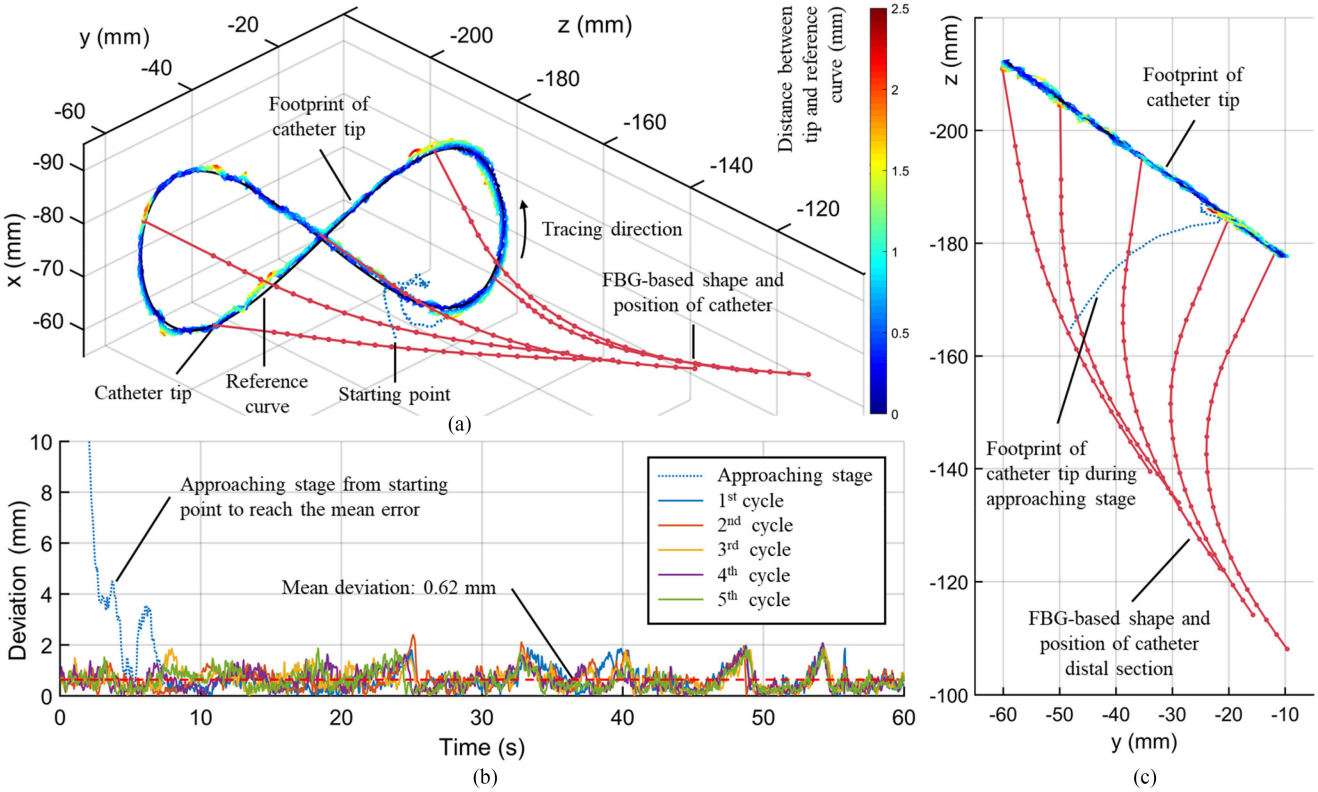

Fig. 12. (a) Catheter tip footprint in five cycles under autonomous path following using the learning-based PCC model. Greater the catheter tip deviation from the reference curve, warmer the color of its tip footprint. The reconstructed catheter shapes and positions were obtained from the proposed shape tracking approach. (b) Deviation from the tip to the reference curve during five cycles. The catheter is controlled to quickly trace the path during the approaching stage. (c) Top view showing the catheter bending shapes at the five instances.

As a comparison, an analytical PCC model was implemented on the robot for a path following task. All the initial parameters of the analytical PCC model and controller remained the same as the proposed model, with the only difference being in the modeling method and absence of the training process. The bending ratios of the three segments were set by constant values, which were obtained by taking average of all the ratios in the training dataset. The footprint recorded by shape tracking system over five cycles is shown in Fig. 13(a). The deviation from tip to reference curve is illustrated in Fig. 13(b), which has an average value of 1.07 mm and a maximum value of 4.27 mm. The average deviations of the two approaches are compared in Fig. 13(c). It can be seen that the path controlled by the analytical PCC model has a larger deviation, which could be attributed to the overestimation of bending by the model. In contrast, the learning-based PCC model could reflect the catheter configuration characteristics more precisely, thus offering a more accurate mapping between the robotic actuation and the tip motion.

F. Ex-Vivo *Tissue Ablation With Pulsatile Flow*

A simulated PVI task with *ex-vivo* tissue ablation was conducted to assess the overall performance of the shape tracking and controller involving external load and tissue interaction. The experiment was performed inside the LA phantom with pulsatile liquid flow. During the task, the catheter was manipulated by the robot to reach the predefined ablation targets on the phantom [see Fig. 14(a)]. A 2-mm tolerance was set for each target. The ablation process was automatically triggered by an RF generator (Biosense Webster Stockert 70) when the catheter tip reached the target region and had tissue contact with impedance $<200\,\Omega$, as introduced in Section IV-C. After conducting ablation at each target point, the robot was reset to the initial position for another targeting process. This reset aimed to separate the catheter tip with the ablated tissue, as well as avoid the collision with the phantom wall during the next targeting.

As shown in Fig. 14(a), the red spheres represent the predefined ablation targets, which have a total number of 15 and are in a volume of $20.9\times23.0\times11.1$ mm^3. These targets form a yellow line corresponding to the circumferential lesion targeted path nearby the pulmonary vein ostia. The footprint (blue line) indicates the targeting motions toward the lesions. In total, 12 out of the 15 (80.0%) lesion targets were successfully reached by the catheter tip to conduct RF ablation. For the unsuccessful cases, the catheter was blocked by the tissue on the targeting path. Fig. 13(b) shows the actual lesion points on the *ex-vivo* tissue. The average time taken to complete the targeting process was 7.76 s, with the average traveling distance of 43.4 mm. The results demonstrate the proposed sensing and feedback control methods enable autonomous RF ablation even in a more dynamic environment with pulsatile liquid flow. In Fig. 14(a), the red curves with dots indicate the reconstructed catheter shape and

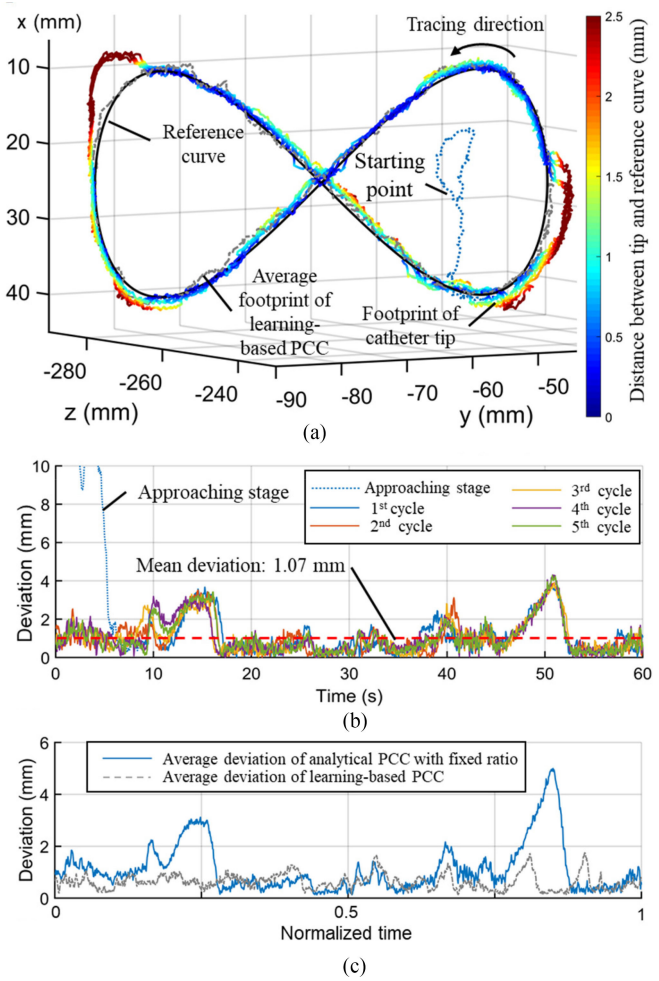

Fig. 13. (a) Catheter tip footprint under autonomous control using the analytical PCC model with fixed bending ratio. Large deviations can be found at the segments with red color. The average footprint of learning-based PCC (dotted gray curve) is overlaid for comparison. (b) Tip deviations from the reference curve. Slow and delayed retracements can be observed at several segments due to inaccurate estimation of the kinematic mapping provided by the analytical PCC model. (c) Average deviations of learning-based PCC and analytical PCC with fixed ratio.

position when the tip reached three of the targets. Other than providing feedback control for the robotic system, the catheter shape tracking can also offer informative visual feedback of the current catheter shape and tip targeting orientation. This additional information could help surgeons keep track of the targeting progress and evaluate the ablation result, thus improving the treatment safety and effectiveness.

G. Tracking and Control Under MRI

To demonstrate the capability of the proposed system under MRI, critical system components were examined by two tests: catheter tracking test and feedback control test. The experiments were conducted in a 1.5 T MRI scanner (SIGNA, GE Healthcare, USA). The setup of the robotic system was illustrated in Fig. 15(a). The slave part of the robot was placed near the MRI scanner bore and connected to the master part through 10-m-long

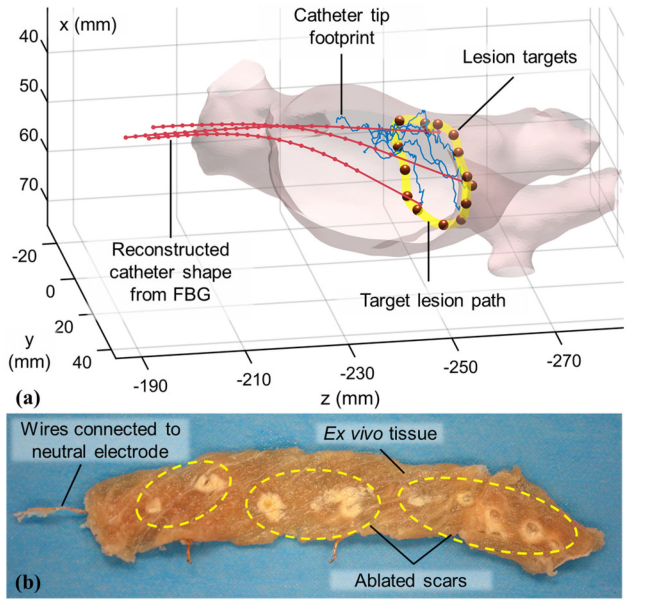

Fig. 14. Results of the PVI task conducted in the LA phantom model. A standard EP catheter was autonomously controlled to reach a series of targets around the pulmonary vein ostium. (a) Front view showing the catheter tip footprint, the targeted ablation points, and the desired lesion path (yellow). The footprint (blue line) indicates the selective tip trajectories toward the targets. (b) Tissue with ablated points (yellow circle).

hydraulic pipelines, which were put through the waveguide in-between the MRI and control rooms. The robotic platform could telemanipulate an MRI compatible cardiac catheter (spec.), which integrated the 12-m-long FBG optic fiber inside the catheter water channel. The optic fiber was channelled through the waveguide as well and connected to the FBG interrogator in control room. Wireless MR tracking coils [38] were attached on the distal bending section of the catheter [see Fig. 15(b)]. The bending section was immersed in water, which could simulate the environment around the catheters in body for MR imaging. The tracking markers were scanned inside an MRI head coil. For the feedback control test, a rigid LA phantom (material) was placed inside the container, with an MR tracking marker attached on the inner surface of the phantom and acted as the target [see Fig. 15(b)].

A catheter tracking test was conducted to validate the 3-D localization using MR tracking markers as well as the fast motion tracking with MR pulse sequence. Such tracking sequence can be interleaved with 2-D anatomical imaging sequence during the EP procedure [58]. Three wireless tracking markers were adopted with continuously performing 2-D imaging during catheter movement. The MR tracking markers are intended to replace the EM tracking markers used in lab-based validations for catheter localization (see Fig. 9). The markers can produce high contrast in comparison to their anatomical surroundings [see Fig. 16(a)] even under low flip-angle excitation, allowing data acquisition with high frequency. Gradient echo sequences, which have the parameters TR/TE = 3.9/1.168 ms, flip angle = 1°, slice thickness = 30 mm, were applied to enable fast 2-D imaging (0.2 s). The slice could cover the three markers and enable 2-D projection imaging [see Fig. 16(a)]. Fig. 16(b) shows

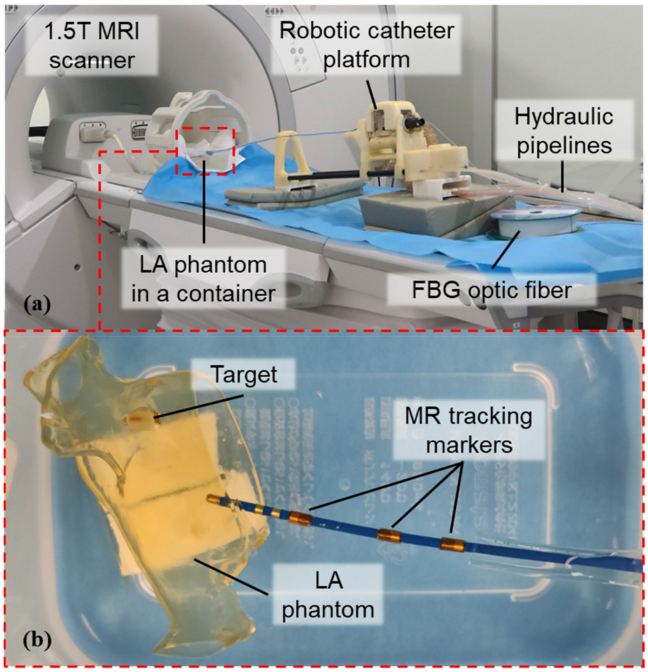

Fig. 15. (a) Setup of the robotic system in MRI room. Pipelines and the FBG fiber were channeled through the waveguide in between the MRI room and control room. (b) MR-compatible EP catheter mounted with three MR tracking markers. Another marker was attached on the inner side of the LA phantom, simulating the lesion target in MR images.

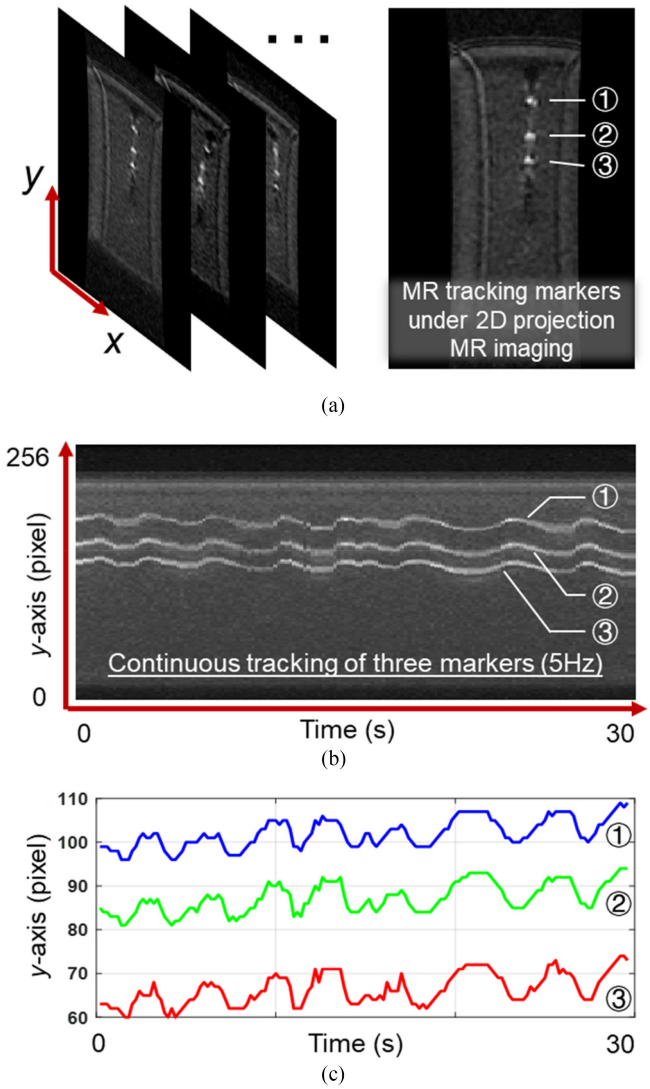

Fig. 16. (a) Three MR markers (①–③) tracked using 2-D projection sequence. (b) Projection of signals to the *y*-axis showing the continuous tracking of the three markers at update rate of 5 Hz. (c) Variations of their corresponding *y*-axis positions over time.

the time series maximum intensity projection along the *y*-axis in a period of 30 s, with a sampling frequency of 5 Hz. In the MR images, the signals of markers had high contrast against the background, which could be automatically detected to provide real-time positional feedback in the MR image coordinate directly [see Fig. 16(c)]. Orthogonal 2-D projection imaging could be further interleaved to achieve 3-D localization of the three markers. However, it should be noted that only the high-contrast signal of tracking markers could be extracted from the images. It is infeasible to continuously extract the catheter location or entire shape from this 2-D image data. On the other hand, the electrode at EP catheter tip can introduce significant (negative) image artifact, which hinders the tracking of tip location from MR imaging. Similarly, MR tracking markers cannot be mounted on the catheter tip due to its artifact.

A feedback control test was carried out to demonstrate the feasibility of the proposed shape tracking method under MRI, using tracking markers and FBG optic fiber. A prescan was taken before the robotic operation to localize the target as well as the MR tracking markets on catheter. The catheter shape obtained by FBG fiber could be registered into the MRI coordinate by matching with the three tracking markers continuously. Through the synergy use of FBGs and the coils, we can achieve accurate shape tracking of catheter in the MRI coordinate. In this way, the catheter tip position in bending direction could be acquired by the FBG fiber in real time, which was used for feedback control of the catheter. During the task, the catheter was automatically manipulated by the robotic platform toward the target. A 3-D MRI scan was performed after the targeting progress, as demonstrated in Fig. 17(a). A virtual catheter, with its shape reconstructed by FBGs, was augmented in the image by matching the signals of MR tracking markers. The footprint of the catheter tip was illustrated in Fig. 17(b), which was generated by combining the shape from FBGs and the robot input in insertion direction. A 3-D volumetric MR image in Fig. 18 illustrates the high-contrast signals of MR tracking markers together with the target. A catheter tip configuration is overlaid in the imaging coordinate by registering the catheter shape with the marker locations. Noted that 3-D localization of the tracking markers and registration of catheter shape in real time are still challenging. Even for the clinical-purpose MRI, the 3-D anatomical imaging is generated by fusing several image clips in different heartbeat cycles, which would take a long time [59]. In our future work, the raw scanning data can be streamed out with an MRI real-time control interface, RTHawk (Heartvista). Then, the shape from FBGs could be registered with the MR tracking markers in real time, providing the shape

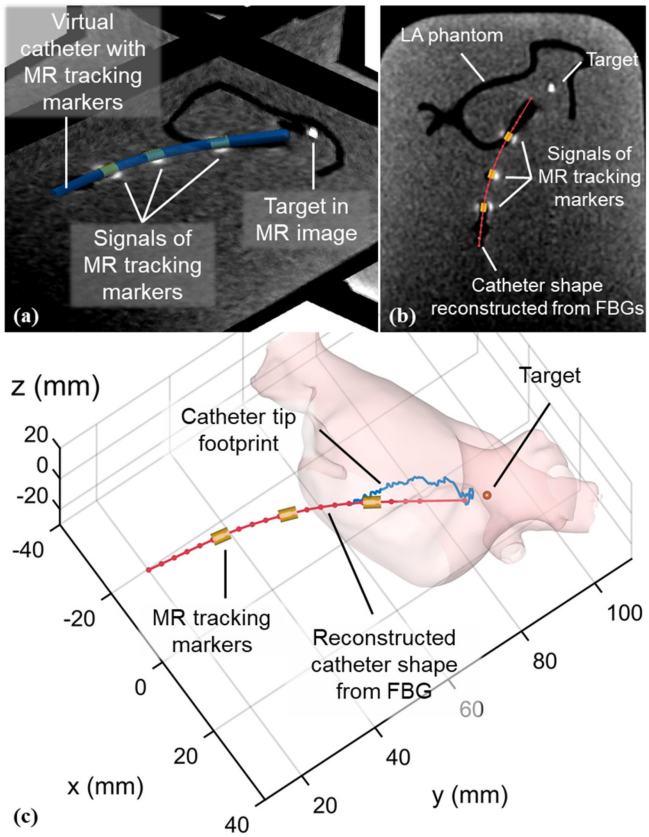

Fig. 17. (a) Location of the three markers on the catheter revealed on MR image slices, along with the lesion fiducial. The catheter configuration reconstructed using FBGs could be registered with the tracked marker locations. (b) Signals of MR tracking markers with FBG-reconstructed catheter shape overlaid. (c) Footprint of the catheter tip plotted in MR image coordinates.

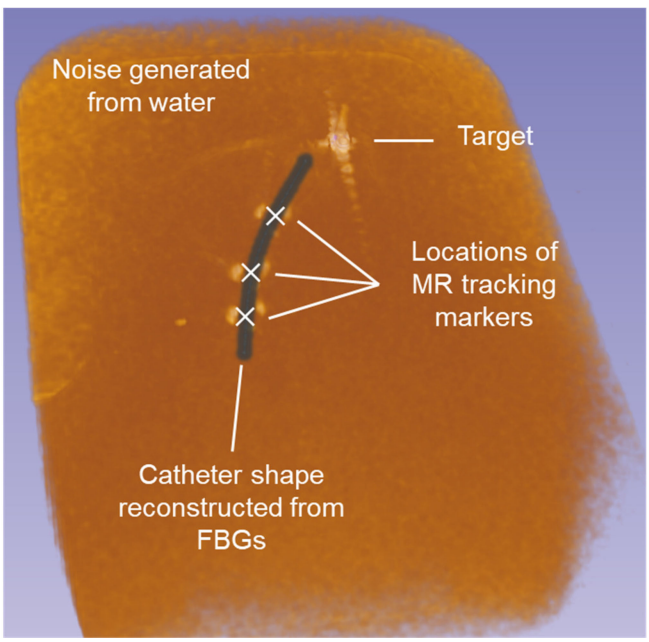

Fig. 18. 3-D volumetric MR image illustrating the high-contrast signals of MR tracking markers together with the target. A catheter tip configuration (in dark) is overlaid in the imaging coordinate by registering the catheter shape with the marker locations.

tracking and feedback control under MRI guidance for validation of the overall efficacy.

VI. Conclusion

In this article, we presented a shape tracking and feedback control method for commercial cardiac catheters during MRI-guided EP procedures. Information from multicore FBG fiber and positional tracking coils was integrated to enable catheter shape estimation under MRI, which was subsequently incorporated with an MR safe catheter robot system. A learning-based modeling method was proposed for the cardiac catheter, with the FBG shape tracking used for system characterization. Comparing with conventional CC or analytical PCC models for continuum robots, the proposed modeling method resolves the modeling uncertainties from heuristic parameter tuning and tendon backlash. The shape sensing using multicore FBG fiber could achieve 2.33° average error for each sensing segment, and 1.53 mm positional accuracy for the catheter tip. Autonomous targeting of five points within the robot workspace showed effective convergence rates (average 16.9 s). Performance of the proposed learning-based PCC and analytic PCC models was compared in a path following task, where the average deviations are 0.62 mm (max. deviation 2.34 mm) and 1.07 mm (max. deviation 4.27 mm), respectively. A study with PVI simulator and *ex-vivo* tissue ablation was conducted to show the overall performance of shape tracking and feedback controller. To demonstrate the capability of the proposed system under MRI, catheter tracking and feedback control tests were conducted in an MRI scanner as well.

In our future work, preclinical animal trials will be conducted to validate the robotic catheter system for MRI-guided EP procedure. RF ablation will be conducted on a live porcine or ovine model with arrhythmia. The proposed shape tracking and controller will be adapted to commercial MR-conditional systems equipped with RF ablation system (e.g., ClearTrace, MRI Interventions, Inc., or Imricor Medical System). The necrosis created by RF ablation, and its efficacy, will also be examined with postmortem histology. It is anticipated that the robotic catheter system would simplify the surgical workflow of MRI-guided EP procedures. The proposed catheter shape tracking method would provide sufficient feedback for visualization and robotic control under MRI, potentially reducing workload of the surgeon as well as postprocedural disease recurrence.

In addition, the proposed FBG-based shape tracking method could be implemented on other MR safe/conditional continuum manipulators for interventional procedures, such as urologic surgery, ophthalmic surgery, and neurosurgery. The direct measurement and reconstruction of shape and position for continuum manipulators would reduce the computational cost of MRI, enabling high-performance feedback control and interactive instrument manipulation. It is believed that both safety and overall operational efficiency would be enhanced, with accurately and intraoperatively updated morphological information of interventional instruments.

REFERENCES

[1] F. Morady, "Radio-frequency ablation as treatment for cardiac arrhythmias," *New England J. Med.*, vol. 340, no. 7, pp. 534–544, 1999.

[2] R. Razavi *et al.*, "Cardiac catheterisation guided by MRI in children and adults with congenital heart disease," *Lancet*, vol. 362, no. 9399, pp. 1877–1882, 2003.

[3] E. J. Schmidt *et al.*, "Electroanatomic mapping and radiofrequency ablation of porcine left atria and atrioventricular nodes using magnetic resonance catheter tracking," *Circulation, Arrhythmia Electrophysiol.*, vol. 2, no. 6, pp. 695–704, 2009.

[4] F. Galassi, D. Brujic, M. Rea, N. Lambert, N. Desouza, and M. Ristic, "Fast and accurate localization of multiple RF markers for tracking in MRI-guided interventions," *Magn. Reson. Mater. Phys., Biol. Med.*, vol. 28, no. 1, pp. 33–48, 2015.

[5] S. Zuehlsdorff *et al.*, "MR coil design for simultaneous tip tracking and curvature delineation of a catheter," *Magn. Reson. Med., Official J. Int. Soc. Magn. Reson. Med.*, vol. 52, no. 1, pp. 214–218, 2004.

[6] R. Ranjan *et al.*, "Identification and acute targeting of gaps in atrial ablation lesion sets using a real-time magnetic resonance imaging system," *Circulation, Arrhythmia Electrophysiol.*, vol. 5, no. 6, pp. 1130–1135, 2012.

[7] M. Grothoff *et al.*, "Magnetic resonance imaging guided transatrial electrophysiological studies in swine using active catheter tracking–experience with 14 cases," *Eur. Radiol.*, vol. 27, no. 5, pp. 1954–1962, 2017.

[8] S. Hilbert *et al.*, "Real-time magnetic resonance-guided ablation of typical right atrial flutter using a combination of active catheter tracking and passive catheter visualization in man: Initial results from a consecutive patient series," *Europace*, vol. 18, no. 4, pp. 572–577, 2016.

[9] B. A. Childers *et al.*, "Use of 3000 Bragg grating strain sensors distributed on four 8-m optical fibers during static load tests of a composite structure," *Proc. SPIE*, vol. 4332, pp. 133–142, 2001.

[10] G. Flockhart, W. MacPherson, J. Barton, J. Jones, L. Zhang, and I. Bennion, "Two-axis bend measurement with Bragg gratings in multicore optical fiber," *Opt. Lett.*, vol. 28, no. 6, pp. 387–389, 2003.

[11] M. J. Paulsen *et al.*, "Development and ex vivo validation of novel force-sensing neochordae for measuring chordae tendineae tension in the mitral valve apparatus using optical fibers with embedded Bragg gratings," *J. Biomech. Eng.*, vol. 142, no. 1, 2020, Art. no. 014501.

[12] K. Mandal, F. Parent, S. Martel, R. Kashyap, and S. Kadoury, "Vessel-based registration of an optical shape sensing catheter for MR navigation," *Int. J. Comput. Assist. Radiol. Surg.*, vol. 11, no. 6, pp. 1025–1034, 2016.

[13] S. C. Ryu and P. E. Dupont, "FBG-based shape sensing tubes for continuum robots," in *Proc. IEEE Int. Conf. Robot. Autom.*, 2014, pp. 3531–3537.

[14] S. C. Ryu *et al.*, "Design of an optically controlled MR-compatible active needle," *IEEE Trans. Robot.*, vol. 31, no. 1, pp. 1–11, Feb. 2015.

[15] N. J. van de Berg, J. Dankelman, and J. J. van den Dobbelsteen, "Design of an actively controlled steerable needle with tendon actuation and FBG-based shape sensing," *Med. Eng. Phys.*, vol. 37, no. 6, pp. 617–622, 2015.

[16] T. Li, A. Pan, and H. Ren, "Reaction force mapping by 3-axis tactile sensing with arbitrary angles for tissue hard-inclusion localization," *IEEE Trans. Biomed. Eng.*, vol. 68, no. 1, pp. 26–35, Jan. 2021.

[17] T. Li, C. Shi, and H. Ren, "Three-dimensional catheter distal force sensing for cardiac ablation based on fiber Bragg grating," *IEEE/ASME Trans. Mechatronics*, vol. 23, no. 5, pp. 2316–2327, Oct. 2018.

[18] K. O. Hill and G. Meltz, "Fiber Bragg grating technology fundamentals and overview," *J. Lightw. Technol.*, vol. 15, no. 8, pp. 1263–1276, Aug. 1997.

[19] Y.-L. Park *et al.*, "Real-time estimation of 3-D needle shape and deflection for MRI-guided interventions," *IEEE/ASME Trans. Mechatronics*, vol. 15, no. 6, pp. 906–915, Dec. 2010.

[20] R. Seifabadi, E. E. Gomez, F. Aalamifar, G. Fichtinger, and I. Iordachita, "Real-time tracking of a bevel-tip needle with varying insertion depth: Toward teleoperated MRI-guided needle steering," in *Proc. IEEE/RSJ Int. Conf. Intell. Robots Syst.*, 2013, pp. 469–476.

[21] R. J. Roesthuis, S. Janssen, and S. Misra, "On using an array of fiber Bragg grating sensors for closed-loop control of flexible minimally invasive surgical instruments," in *Proc. IEEE/RSJ Int. Conf. Intell. Robots Syst.*, 2013, pp. 2545–2551.

[22] R. J. Roesthuis and S. Misra, "Steering of multisegment continuum manipulators using rigid-link modeling and FBG-based shape sensing," *IEEE Trans. Robot.*, vol. 32, no. 2, pp. 372–382, Apr. 2016.

[23] H. Rafii-Tari *et al.*, "Objective assessment of endovascular navigation skills with force sensing," *Ann. Biomed. Eng.*, vol. 45, no. 5, pp. 1315–1327, 2017.

[24] N. Kumar, J. Wirekoh, S. Saba, C. N. Riviere, and Y.-L. Park, "Soft miniaturized actuation and sensing units for dynamic force control of cardiac ablation catheters," *Soft Robot.*, vol. 8, pp. 59–70, 2021.

[25] M. C. Yip, J. A. Sganga, and D. B. Camarillo, "Autonomous control of continuum robot manipulators for complex cardiac ablation tasks," *J. Med. Robot. Res.*, vol. 2, no. 1, 2017, Art. no. 1750002.

[26] S. B. Kesner and R. D. Howe, "Position control of motion compensation cardiac catheters," *IEEE Trans. Robot.*, vol. 27, no. 6, pp. 1045–1055, Dec. 2011.

[27] S. Hasanzadeh and F. Janabi-Sharifi, "Model-based force estimation for intracardiac catheters," *IEEE/ASME Trans. Mechatronics*, vol. 21, no. 1, pp. 154–162, Feb. 2016.

[28] T. L. T. Lun, K. Wang, J. D. L. Ho, K.-H. Lee, K. Y. Sze, and K.-W. Kwok, "Real-time surface shape sensing for soft and flexible structures using fiber Bragg gratings," *IEEE Robot. Autom. Lett.*, vol. 4, no. 2, pp. 1454–1461, Apr. 2019.

[29] S. Sefati, F. Alambeigi, I. Iordachita, M. Armand, and R. J. Murphy, "FBG-based large deflection shape sensing of a continuum manipulator: Manufacturing optimization," in *Proc. IEEE SENSORS*, 2016, pp. 1–3.

[30] R. G. Duncan *et al.*, "OFDR-based distributed sensing and fault detection for single-and multi-mode avionics fiber-optics," in *Proc. Joint Conf. Aging Aircr.*, 2007, pp. 16–19.

[31] H. Murayama, H. Igawa, K. Omichi, and Y. Machijima, "Distributed sensing with OFDR and its application to structural health monitoring," in *Proc. 21st Int. Conf. Opt. Fiber Sensors*, 2011, vol. 7753, Art. no. 775305.

[32] D. Tosi, "Review of chirped fiber Bragg grating (CFBG) fiber-optic sensors and their applications," *Sensors*, vol. 18, no. 7, 2018, Art. no. 2147.

[33] B. A. Childers, D. K. Gifford, R. G. Duncan, M. T. Raum, M. E. Vercellino, and M. E. Froggatt, "Fiber optic position and shape sensing device and method relating thereto," Patent US7 781 724, Aug. 24, 2010.

[34] C. Shi, S. Giannarou, S.-L. Lee, and G.-Z. Yang, "Simultaneous catheter and environment modeling for trans-catheter aortic valve implantation," in *Proc. IEEE/RSJ Int. Conf. Intell. Robots Syst.*, 2014, pp. 2024–2029.

[35] S. Jäckle, T. Eixmann, H. Schulz-Hildebrandt, G. Hüttmann, and T. Pätz, "Fiber optical shape sensing of flexible instruments for endovascular navigation," *Int. J. Comput. Assist. Radiol. Surg.*, vol. 14, no. 12, pp. 2137–2145, 2019.

[36] C. L. Dumoulin, S. Souza, and R. Darrow, "Real-time position monitoring of invasive devices using magnetic resonance," *Magn. Reson. Med.*, vol. 29, no. 3, pp. 411–415, 1993.

[37] Y. Chen *et al.*, "Design and fabrication of MR-tracked metallic stylet for gynecologic brachytherapy," *IEEE/ASME Trans. Mechatronics*, vol. 21, no. 2, pp. 956–962, Apr. 2016.

[38] C.-L. Cheung, J. D.-L. Ho, V. Vardhanabhuti, H.-C. Chang, and K.-W. Kwok, "Design and fabrication of wireless multilayer tracking marker for intraoperative MRI-guided interventions," *IEEE/ASME Trans. Mechatronics*, vol. 25, no. 2, pp. 1016–1025, Apr. 2020.

[39] Z. Guo *et al.*, "Compact design of a hydraulic driving robot for intraoperative MRI-guided bilateral stereotactic neurosurgery," *IEEE Robot. Autom. Lett.*, vol. 3, no. 3, pp. 2515–2522, Jul. 2018.

[40] Z. He *et al.*, "Design of a percutaneous MRI-guided needle robot with soft fluid-driven actuator," *IEEE Robot. Autom. Lett.*, vol. 5, no. 2, pp. 2100–2107, Apr. 2020.

[41] M. A. Rube, A. B. Holbrook, B. F. Cox, J. G. Houston, and A. Melzer, "Wireless MR tracking of interventional devices using phase-field dithering and projection reconstruction," *Magn. Reson. Imag.*, vol. 32, no. 6, pp. 693–701, 2014.

[42] K.-H. Lee *et al.*, "MR safe robotic manipulator for MRI-guided intracardiac catheterization," *IEEE/ASME Trans. Mechatronics*, vol. 23, no. 2, pp. 586–595, Apr. 2018.

[43] Y. Ganji and F. Janabi-Sharifi, "Catheter kinematics for intracardiac navigation," *IEEE Trans. Biomed. Eng.*, vol. 56, no. 3, pp. 621–632, Mar. 2009.

[44] X. Wang *et al.*, "Experimental validation of robot-assisted cardiovascular catheterization: Model-based versus model-free control," *Int. J. Comput. Assist. Radiol. Surg.*, vol. 13, no. 6, pp. 797–804, 2018.

[45] T. Liu and M. C. Çavuşoğlu, "Three dimensional modeling of an MRI actuated steerable catheter system," in *Proc. IEEE Int. Conf. Robot. Autom.*, 2014, pp. 4393–4398.

[46] M. B. Rubin, *Cosserat Theories: Shells, Rods and Points*. Dordrecht, Netherlands: Springer Netherlands, 2013.

[47] Y. Ganji and F. Janabi-Sharifi, "Kinematic characterization of a cardiac ablation catheter," in *Proc. IEEE/RSJ Int. Conf. Intell. Robots Syst.*, 2007, pp. 1876–1881.

[48] R. J. Webster and B. A. Jones, "Design and kinematic modeling of constant curvature continuum robots: A review," *Int. J. Robot. Res.*, vol. 29, no. 13, pp. 1661–1683, 2010.
[49] M. Barkagan, M. Rottmann, E. Leshem, C. Shen, A. E. Buxton, and E. Anter, "Effect of baseline impedance on ablation lesion dimensions: A multimodality concept validation from physics to clinical experience," *Circulation, Arrhythmia Electrophysiol.*, vol. 11, no. 10, 2018, Art. no. e006690.
[50] K. W. Kwok, Z. Dong, Z. Guo, K. C. D. Fu, K. H. Lee, and C. L. Cheung, "Robotic catheter system for MRI-guided cardiovascular interventions," Patent US15/630,406; PCT/CN2017/089701, Jun. 22, 2017.
[51] Z. Dong *et al.*, "High-performance continuous hydraulic motor for MR safe robotic teleoperation," *IEEE Robot. Autom. Lett.*, vol. 4, no. 2, pp. 1964–1971, Apr. 2019.
[52] Y. Fan, K.-W. Kwok, Y. Zhang, G. S.-H. Cheung, A. K.-Y. Chan, and A. P.-W. Lee, "Three-dimensional printing for planning occlusion procedure for a double-lobed left atrial appendage," *Circulation, Cardiovasc. Interventions*, vol. 9, no. 3, 2016, Art. no. e003561.
[53] B. K. Foucha, "The ABCs of A to V: Right atrial/left atrial (PCW) pressures," *CathLab Dig.*, vol. 17, no. 5, May 2009. [Online]. Available: https://www.hmpgloballearningnetwork.com/site/cathlab/articles/the-abcs-a-v-right-atrial-left-atrial-pcw-pressures
[54] S. Nakatani *et al.*, "Noninvasive assessment of left atrial maximum dP/dt by a combination of transmitral and pulmonary venous flow," *J. Amer. College Cardiol.*, vol. 34, no. 3, pp. 795–801, 1999.
[55] M. J. Gander *et al.*, "Measurement of bending in two dimensions using multicore optical fibre," in *Proc. Eur. Workshop Opt. Fibre Sensors*, 1998, vol. 3483, pp. 64–68.
[56] K. Bronnikov *et al.*, "Durable shape sensor based on FBG array inscribed in polyimide-coated multicore optical fiber," *Opt. Express*, vol. 27, no. 26, pp. 38421–38434, 2019.
[57] C. G. Robinson *et al.*, "Phase I/II trial of electrophysiology-guided noninvasive cardiac radioablation for ventricular tachycardia," *Circulation*, vol. 139, no. 3, pp. 313–321, 2019.
[58] D. R. Elgort, E. Y. Wong, C. M. Hillenbrand, F. K. Wacker, J. S. Lewin, and J. L. Duerk, "Real-time catheter tracking and adaptive imaging," *J. Magn. Reson. Imag., Official J. Int. Soc. Magn. Reson. Med.*, vol. 18, no. 5, pp. 621–626, 2003.
[59] Y. Amano *et al.*, "Three-dimensional cardiac MR imaging: Related techniques and clinical applications," *Magn. Reson. Med. Sci.*, vol. 16, no. 3, pp. 183–189, 2017.

Ziyang Dong received the B.Eng. degree in building services engineering from The Hong Kong Polytechnic University, Hong Kong, in 2014, and the M.S. and Ph.D. degrees in mechanical engineering from The University of Hong Kong, Hong Kong, in 2015 and 2020, respectively.

His research interests include design and control of surgical robotic systems, MR safe/conditional robotic systems, and devices for cardiac catheterization.

Dr. Dong has a coauthored paper recognized with the Best Conference Paper Award of the IEEE International Conference on Robotics and Automation in 2018.

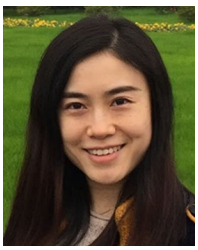

Xiaomei Wang (Member, IEEE) received the B.E. degree in automation from the Harbin Institute of Technology, Harbin, China, in 2014, the M.E. degree in control science and engineering from the Shenzhen Graduate School, Harbin Institute of Technology, Shenzhen, China, in 2016, and the Ph.D. degree in robotics from The University of Hong Kong, Hong Kong, in 2020.

She is currently a Postdoctoral Fellow with the Department of Mechanical Engineering, The University of Hong Kong. Her research interests include learning-based robot control and sensing, surgical robotics, and continuum robot control.

Dr. Wang is an Associate Editor for the IEEE International Conference on Robotics and Automation 2022 and RoboSoft 2022, and an Area Chair for the Conference on Information Processing in Computer-Assisted Interventions 2022.

Ge Fang received the bachelor's degree in mechanical engineering and automation from the Huazhong University of Science and Technology, Wuhan, China, in 2014, the master's degree in mechanical engineering from Shanghai Jiao Tong University, Shanghai, China, in 2017, and the Ph.D. degree in robotics from The University of Hong Kong, Hong Kong, in 2021.

His research interests include magnetic resonance imaging guided robotics system, soft robotics, and learning-based robot control.

Zhuoliang He received the M.S. degree in engineering from Zhejiang University, Hangzhou, China, in 2018. He is currently working toward the Ph.D. degree in medical robotics with The University of Hong Kong, Hong Kong.

His research interests include robotic mechanism design, surgical robotics, magnetic resonance imaging guided robotic systems, and robotic instrument for endoscopic surgeries.

Justin Di-Lang Ho received the bachelor's degree in mechatronic engineering from The University of Queensland, Brisbane, QLD, Australia, in 2016, and the Master of Philosophy degree in the field of robotics from the Department of Mechanical Engineering, The University of Hong Kong, Hong Kong, in 2019.

His current research focuses on minimally invasive surgical robotics, including magnetic resonance imaging guided robotics and miniature robotic instruments.

Chim-Lee Cheung received the B.Eng. degree in electrical engineering, in 2015, from The University of Hong Kong, Hong Kong, where he is currently working toward the Ph.D. degree in medical robotics.

His research interests include the design and fabrication of radiofrequency positional tracking markers for intraoperative magnetic resonance imaging guided navigation and robotic systems.

Wai Lun Tang received the B.Eng. degree in mechanical engineering from Royal Melbourne Institute of Technology University, Melbourne, VIC, Australia, in 2020.

From 2016 to 2021, he was a Research Assistant with the Department of Mechanical Engineering, The University of Hong Kong, Hong Kong. His research interests include robotic mechanism design, soft robot design and fabrication, and robotic actuation system.

Xiaochen Xie (Member, IEEE) received the B.E. degree in automation and M.E. degree in control science and engineering from the Harbin Institute of Technology, Harbin, China, in 2012 and 2014, respectively, and the Ph.D. degree in control engineering from The University of Hong Kong, Hong Kong, in 2018.

From 2018 to 2021, she was a Postdoctoral Fellow with The University of Hong Kong. Her research interests include robust control and filtering, periodic systems, switched systems, intelligent systems, robotics and process monitoring.

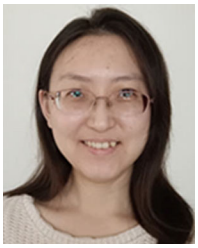

Liyuan Liang received the bachelor's degree in electronic science and technology from Beijing Normal University, Beijing, China, in 2017. She is currently working toward the Ph.D. degree in magnetic resonance imaging with The University of Hong Kong, Hong Kong.

Her research interests include magnetic resonance imaging reconstruction and motion correction.

Hing-Chiu Chang received the B.S. and M.S. degrees in electrical engineering from the National Taiwan University, Taipei, Taiwan, in 2004 and 2006, respectively, and the Ph.D. degree in biomedical electronics from the Graduate Institute of Biomedical Electronics and Bioinformatics, National Taiwan University, in 2012.

He spent six years working for a medical imaging industry to develop imaging techniques for research. He is currently an Assistant Professor with the Department of Diagnostic Biomedical Engineering, The Chinese University of Hong Kong, Hong Kong. His research interests include image reconstruction and artifact reduction for fast magnetic resonance imaging.

Chi Keong Ching received the Bachelor of Medicine and Surgery degree in medicine from the National University of Singapore, Singapore, in 1995. He subsequently obtained the Membership of the Royal College of Physicians, London, U.K., in 2001, and the Certificate of Specialist Accreditation (Cardiology) in 2004. He completed his Clinical Fellowship in Cardiac Electrophysiology and Pacing from the Cleveland Clinic, Cleveland, OH, USA, in 2007.

He is currently a Senior Consultant with the Department of Cardiology, and also the Director of Cardiac Electrophysiology and Pacing with the National Heart Centre Singapore, Singapore. He is also a Clinical Associate Professor with the Duke-NUS Medical School, Singapore. His subspecialty interest is in cardiac electrophysiology and pacing.

Prof. Ching has been selected as a Fellow of the ASEAN Society of Cardiology, Fellow of the Academy of Medicine (Singapore), and Fellow of the Heart Rhythm Society, USA, in recognition of his professional and research achievements.

Ka-Wai Kwok (Senior Member, IEEE) received the B.Eng. and M.Phil. degrees in automation and computer-aided engineering from the Chinese University of Hong Kong, Hong Kong, in 2003 and 2005, respectively, and the Ph.D. degree in computing from the Hamlyn Center for Robotic Surgery, Department of Computing, Imperial College London, London, U.K., in 2012.

He is currently an Associate Professor with the Department of Mechanical Engineering, The University of Hong Kong (HKU), Hong Kong. Prior to joining HKU in 2014, he was a Postdoctoral Fellow with the Imperial College London in 2012 for surgical robotics research. In 2013, he was awarded the Croucher Foundation Fellowship, which supported his research jointly supervised by advisors from the University of Georgia, Athens, GA, USA, and Brigham and Women's Hospital, Harvard Medical School, Boston, MA, USA. His research interests include surgical robotics, intraoperative image processing, and their uses of intelligent and control systems.

Dr. Kwok is as an Associate Editor for *Journal of Systems and Control Engineering*, IEEE ROBOTICS AND AUTOMATION MAGAZINE, and *Annals of Biomedical Engineering*. He is the Principal Investigator of research group for Interventional Robotic and Imaging Systems, HKU. To date, he has coauthored 123 publications with $>$50 clinical fellows and $>$90 engineering scientists, and six out of 14 invention patents licensed/transferred to industrial partners in support for their commercialization. His multidisciplinary work has been recognized by $>$10 international publication awards, mostly under IEEE, particularly in the largest flagship conferences of robotics, e.g., ICRA Best Conference Paper Award in 2018, and IROS Toshio Fukuda Young Professional Award in 2020.